5-1-2012

The behavior of zircon during partial melting in anatectic migmatites: Insights to metamorphism, deformation and tectonism in the central Santa Fe Range, northern New Mexico

Michelle Renee Stropky
University of Nevada, Las Vegas, stropkym@gmail.com

THE BEHAVIOR OF ZIRCON DURING PARTIAL MELTING IN ANATECTIC MIGMATITES: INSIGHTS TO METAMORPHISM, DEFORMATION AND TECTONISM IN THE CENTRAL SANTA FE RANGE, NORTHERN NEW MEXICO

By

Michelle Renee Stropky

Bachelor of Science
Environmental Geology
University of Nevada, Las Vegas
December 2008

A thesis submitted in partial fulfillment
of the requirements for the

Master of Science Degree in Geoscience

Department of Geoscience
College of Sciences
The Graduate College

University of Nevada, Las Vegas
May 2012

THE GRADUATE COLLEGE

We recommend the thesis prepared under our supervision by

Michelle Renee Stropky

entitled

The Behavior of Zircon During Partial Melting in Anatectic Migmatites: Insights to Metamorphism, Deformation and Tectonism in the Central Santa Fe Range, Northern New Mexico

be accepted in partial fulfillment of the requirements for the degree of

Masters of Science in Geoscience
Department of Geoscience

Rodney Metcalf, Ph.D., Committee Chair

Terry Spell, Ph.D., Committee Member

Eugene Smith, Ph.D., Committee Member

Vernon Hodge, Ph.D., Graduate College Representative

Ronald Smith, Ph. D., Vice President for Research and Graduate Studies
and Dean of the Graduate College

May 2012

ABSTRACT

THE BEHAVIOR OF ZIRCON DURING PARTIAL MELTING IN ANATECTIC MIGMATITES: INSIGHTS TO METAMORPHISM, DEFORMATION AND TECTONISM IN THE CENTRAL SANTA FE RANGE NORTHERN NEW MEXICO

By

Michelle Renee Stropky

Dr. Rodney V. Metcalf, Examination Committee Chair

Professor of Geology

University of Nevada, Las Vegas

Three lithologic assemblages exposed in the central Santa Fe Range, northern New Mexico include (1) a septum of Proterozoic low temperature (~700^{o}C, 5.5 kbars), semi-pelitic anatectic migmatites surrounded by (2) deformed megacrystic biotite granite that is intruded by (3) discrete plutons of largely undeformed hornblende biotite tonalite. Metamorphic fabrics in the migmatite record three deformation events (D_1 – D_3); a composite S_1/S_2 fabric (D_1 and D_2) that formed contemporaneous with anatexis and is folded about a southwest plunging map-scale (D_3) antiform. The megacrystic granite exhibits a pervasive S_1 subsolidus foliation that parallels the S_1/S_2 fabric in the migmatite and is cut by discordant leucosomes. The hornblende tonalite cross-cuts both the S_1 foliation of the megacrystic granite and the S_1/S_2 foliation of the migmatite. New U-Pb SIMS ages were collected on zircon from the two plutonic units and from a stromatic metasedimentary migmatite (leucosome-melanosome-paleosome). Megacrystic granite yielded a concordant U-Pb age of 1633 ± 12 Ma (2σ) and hornblende tonalite yielded a concordant U-Pb age of 1395 ± 7 Ma (2σ); both plutonic units have Th/U >0.1. The evaluation of migmatite zircon from leucosome-melanosome-paleosome have highly variable Th/U values (>0.1 to <0.01) and uranium concentrations (200 – 9,000ppm). Migmatite zircon with Th/U >0.1 yielded two age

populations: protolith cores with a Pb-Pb age = 1634 ± 16 Ma and new growth with a Pb-Pb age of 1398 ± 17 Ma. Three zircon analyses yield older Pb-Pb ages of 1791 ± 25 Ma. Migmatite zircon with Th/U values <0.1 yield mixed Pb-Pb ages between 1.6 – 1.4 Ga that have elevated Ca, Fe, and Al concentrations, suggesting zircon recrystallization from fluids and/or melts; such zircon is primarily found in leucosome and may represent fluid released during melt crystallization. Older migmatite zircon ages are interpreted as being inherited from a metasedimentary protolith and younger migmatite zircon ages at 1399 Ma represents the age of anatexis and deformation (this includes deformation of the 1633 Ma megacrystic biotite granite). Statistical correlation of both the migmatite and tonalite ages suggests mafic magmatism enhanced regional metamorphism and supports studies documenting metamorphism, deformation and tectonism across the Laurentian margin at ~1.4 Ga.

ACKNOWLEDGEMENTS

I would first like to thank all of the institutions and organizations for their financial support towards this project. Without their funding this project would not have been possible. Much appreciation is made to the University of Nevada, Las Vegas Geoscience Department for funding two term scholarships, the UNLV Graduate and Professional Student Association grant, the Geological Society of America grant, and the Mineralogical Society of America grant in providing financial support for this project.

I would also like to extend many thanks to Dr. Rodney Metcalf for his advisement and project development. Without your advisement and faith in me this project would not have been possible, you knew when to push me and were always there during the ups and downs. I cannot thank you enough for all of your encouragement; this experience has allowed me to grow as both a person and as a scientist and will be carried with me throughout the rest of my life.

I also want to extend my thanks towards all the great geoscientists that assisted with data collection and project collaboration. Thanks is made to my advisory committee Dr. Terry Spell, Dr. Eugene Smith, and to Dr. Vernon Hodge. Appreciation is also made to Dr. Sean Mulcahy for Cathodoluminescence imagery and zircon sample preparation; to Christopher Adcock for Electron Backscatter Detection analyses; and to Axel Schmitt for Secondary Ion Mass Spectrometry analysis and zircon sample preparation.

Lastly I cannot thank my friends and family enough for their encouragement and support throughout this entire process, especially to Robert E. Davis. Without your support and love this never would have been possible and I thank you for that.

TABLE OF CONTENTS

LIST OF TABLES

LIST OF FIGURES

CHAPTER 1: INTRODUCTION

Zircon studies in anatectic migmatites can provide chronological constraints of protoliths and document crustal melting, as well as constrain ages for structures, deformation and high grade metamorphism related to orogenesis. Understanding zircon behavior in anatectic migmatites is important for correct interpretation of ages that document timing of metamorphism, deformation and anatexis. The importance in recognizing zircon alteration by hydrothermal fluids and subsequently understanding of zircon behavior during high-grade metamorphism to correctly interpret the U-Pb isotopic system is widely recognized (Geisler et al., 2007; Hoskin and Black, 2000).

Anatectic migmatites are found in the central Santa Fe Range of northern New Mexico where the most critical aspect of northern New Mexico tectonic history concerns the age of tectonism and metamorphism. Regional metamorphism and deformation of the southwestern US is primarily defined by three Precambrian provinces, the (1) Mojave (2.0 to 1.8 Ga volcanic arcs built on older crust), (2) Yavapai (1.8 to 1.7 Ga juvenile arc crust) and (3) Mazatzal (1.7 to 1.6 Ga juvenile crust) (Karlstrom et al., 2001; Karlstrom et al., 2004; Williams et al., 1999; Daniel et al., 1995). These provinces, that were located in southwestern Laurentia, span more than nine states, including Utah, Arizona, Wyoming, Colorado, and New Mexico. Proterozoic rocks within the New Mexico region record lithospheric continental evolution of southwestern Laurentia and have been used to provide important insights to tectonics and geodynamics that include how deformation, metamorphism, and plutonism interact with each other during orogenic events and causes of 1.4 Ga intracratonic A-type magmatism and tectonism (Karlstrom et al., 2004). However, deformation fabrics vary by style and intensity across the region and a major problem for creating a regional tectonic model is correlating fabrics, fold generations, and deformational events between study areas (Williams et al., 1999).

This paper addresses the timing of metamorphism, deformation and tectonism in the Santa Fe Range, northern New Mexico and relates observations and conclusions to the local and regional Proterozoic history of the southwest. Three lithologic assemblages are exposed in the central Santa Fe Range, northern New Mexico: (1) a septum of Proterozoic low temperature

(~700^{o}C, 5.5 kbars), semi-pelitic anatectic migmatites surrounded by (2) deformed megacrystic biotite granite that is intruded by (3) discrete plutons of largely undeformed hornblende biotite tonalite. This study used SIMS U-Pb isotopic dating of zircon to constrain ages for the two plutonic units and migmatite, providing additional insights to the local and regional metamorphic and tectonic history of the central Santa Fe Range of northern New Mexico. In addition this study addressed the behavior of zircon during partial melting in anatectic migmatites to understand how anatexis and migmatization affected the U-Pb isotopic system.

CHAPTER 2: GEOLOGIC SETTING

Paleoproterozoic rocks of northern New Mexico are part of a 1,200-km-wide series of northeast-trending orogenic belts (Karlstrom et al., 2004; Williams et al., 1999). Tectonic and petrologic studies suggest accretion of predominantly juvenile continental material in volcanic arcs along with assembly and stabilization of diverse terrains onto North America from 1.8 Ga to 1.6 Ga. Three major crustal provinces (Figure 1) are defined and bounded by generally sub-vertical regional shear zones, where the provinces include metavolcanic, metasedimentary, and plutonic rocks; these provinces are the (1) 2.0 Ga to 1.8 Ga Mojave province, (2) 1.8 Ga to 1.7 Ga Yavapai province, and (3) 1.7 Ga to 1.6 Ga Mazatzal province (Karlstrom et al., 2004). Karlstrom et al. (2004) uses the terms Yavapai and Mazatzal orogeny to describe orogenic events associated with the Yavapai and Mazatzal crustal provinces as follows: (1) the Yavapai orogeny describes the accretion of arc crust from 1.8 Ga to 1.7 Ga, and includes 1.78 Ga to 1.72 Ga arc development and collisions and an orogenic peak at ~1.7 Ga that resulted in amalgamation of Yavapai crust to Laurentia, and (2) the Mazatzal orogeny describes accretion of 1.67 Ga to 1.65 Ga crust to southern Laurentia with peak deformation occurring at ~1.65 Ga that affected both Yavapai and Mazatzal crust. During this time of crustal amalgamation and orogenic progression, several pulses of deformation and metamorphism took place. The most clearly recorded evidence of deformation and metamorphism in the Yavapai province occurs in northern Colorado and in the Upper Granite Gorge in the Grand Canyon of Arizona (Shaw & Karlstrom, 1999; Whitmeyer & Karlstrom, 2007). Mazatzal deformation and metamorphism is most clearly recorded in southeastern Arizona and south of the Santa Fe Range in southern New Mexico. A broad transition zone between the Yavapai and Mazatzal provinces is recognized in southern Colorado and northern New Mexico (Figure 1) where it has been difficult to clearly differentiate between Yavapai age and Mazatzal age metamorphism and deformation.

Deformation and metamorphism occurred between 1.72 Ga and 1.65 Ga within the Yavapai-Mazatzal transition zone in New Mexico. According to Williams et al. (1999) the oldest lithotectonic sequence in New Mexico consists of 1.76 Ga to 1.72 Ga metamorphosed mafic

volcanic rocks and suites of diverse metaplutonic rocks (Figure 2); the second sequence contains both metasedimentary and felsic metavolcanic rocks of the 1.72 Ga to 1.69 Ga Vadito Group which overlies the mafic sequences and locally contain moderately to strongly deformed granitoids (1.7 Ga to 1.65 Ga). The 1.7 Ga to 1.69 Ga quartzites and pelitic schists of the Hondo Group overlies the Vadito Group and is the youngest sequence in the transition zone. An "anorogenic granite suite" of mildly deformed 1.48 Ga to 1.35 Ga granitoids (Anderson, 1989) and pegmatites are widely exposed throughout several New Mexico ranges. Excluding the ca. 1.4 Ga granitoids, all of the Proterozoic rocks have experienced multiple deformation events where at least three deformation phases are interpreted in most exposed areas (Williams et al., 1999). Several studies have concluded primary regional deformation and metamorphism in the New Mexico transition zone occurred primarily during the 1.65 Ga Mazatzal orogeny (Williams, 1990; Bauer and Williams, 1994). However, more recent research by Bauer et al. (1993), Bishop (1997) and Wingsted (1997) support evidence of intense metamorphism and deformation at 1.4 Ga.

Figure 3 illustrates an age-probability plot of U-Pb zircon ages for the New Mexico region (Karlstrom et al., 2004) where 1.8 Ga to 1.6 Ga assembly associated with the Yavapai and Mazatzal crust and regional 1.48 Ga to 1.35 Ga intracratonic magmatism and tectonism is separated by a tectonic lull from 1.6 Ga to 1.48 Ga. During this period there is a nearly complete absence of recorded isotopic ages, including a lack of documented magmatism and/or metamorphism within the region. This tectonic lull has been interpreted as being a time of crustal stability of the North American craton. The 1.55 Ga to 1.35 Ga Granite-Rhyolite province, located to the southeast of the Mazatzal province (Figure 1), records reactivated tectonism with accretion of juvenile arc crust where a protracted interval of Mesoproterozoic (1.48 Ga to 1.35 Ga) plutonism affected portions of both the Yavapai and Mazatzal crustal provinces (Karlstrom et al., 2004). The 1.48 Ga to 1.35 Ga plutons are dominated by K-feldspar megacrystic granites with metaluminous A-type compositions, and have been referred to as "anorogenic" due to a perceived lack of 1.4 Ga deformation (Anderson, 1983; Anderson and Bender, 1989).

Williams et al. (1999) designates three fabric forming deformation stages designated D_1 – D_3 that are preserved in Yavapai-age supracrustal rocks, where evidence is observed in structures (thrust shear zones and F_2 – F_3 folds) and in metamorphic fabrics (S_1 – S_3). The D_1 event is recorded in S_1 layer parallel foliations. The D_2 event is recorded in outcrop to map scale F_2 folds that are defined by folded layering and S_1 and by an axial planar S_2 foliation evident in fold hinges but parallel to S_1 in fold limbs. Many of the map scale F_2 folds are also bounded by thrust shear zones. The dominant regional foliation is S_2 and is present in Yavapai-age (1.68 to 1.65 Ga) granitic rocks as a gneissic deformation fabric. The D_3 event is recorded in open upright folds and in a weak sub-vertical S_3 crenulation cleavage. The ~1.43 Ga granite plutons are largely undeformed and 1.43 Ga pegmatite dikes cut D_3 folds and fabrics. Most direct attempts to date metamorphism come from D_3 porphyroblasts and yield ages of about 1.4 Ga (U-Pb) to 1.2 Ga ($^{40}Ar/^{39}Ar$, Williams et al. 1999) which has raised questions about the role of 1.4 Ga tectonism in the crustal evolution of the southwest.

Aspen Basin study area: The Aspen Basin study suite in the central Santa Fe Range contains Proterozoic rocks that occur within the southern transition zone between the Yavapai and Mazatzal crustal provinces. The study suite lies within the Santa Fe Baldy batholith and is bounded by the Pecos-Picuris fault to the east and the Borrego fault to the west (Figure 2). Proterozoic supracrustal rocks within the batholith include metagreywacke and metavolcanic rocks (Metcalf 1990). As shown in Figure 4, Metcalf (1990) mapped plutonic rocks into five separate map units but grouped them into (1) an older, pre-kinematic felsic group containing the megacrystic biotite granite and megacrystic granite units with gradational contacts, and (2) a younger, post-kinematic (undeformed) mafic group mapped as discrete plutonic bodies of hornblende quartz diorite, hornblende biotite tonalite, and biotite tonalite. Metcalf (1990) also mapped a suite of migmatitic supracrustal rocks that include the amphibolite gneiss, felsic gneiss and biotite gneiss units, and are anatectic in origin. The biotite gneiss includes two types of migmatite, a schlieren type with granitic leucosomes and a stromatic (layered) type with trondhjemitic leucosomes. The research focuses on the stromatic type migmatites as this suite most closely approximates in situ neosomes (newly formed material). The Aspen Basin

migmatites formed under peak metamorphic conditions of 604 – 680 ^{o}C and 5.2 – 5.5 kbars (Metcalf, 1990), where there was syn-kinematic localized partial melting and leucosome-melanosome segregation. Metcalf (1990) recognized metamorphic fabrics in the migmatites that record D_1 – D_3 events similar to that discussed by Williams et al. (1999) across much of New Mexico. The D_1 and D_2 events are recorded by a composite S_1/S_2 fabric and this fabric is folded about a map-scale (F_3 – D_3) antiform (Figure 4).

The Santa Fe Range lies within and at the southern extent of the Yavapai-Mazatzal transition zone. While the Proterozoic age of rocks of the central Santa Fe Range has been recognized, geochronological data for the plutonic and migmatitic rocks are lacking. Dating of the migmatitic biotite gneiss, megacrystic biotite granite and hornblende biotite tonalite units have provided ages that constrain the timing of deformation, metamorphism, and plutonism within the region, and has provided additional evidence of 1.6 Ga and 1.4 Ga deformation, metamorphism and tectonism associated with the Proterozoic history of northern New Mexico. This study addresses the age of crystallization of the (1) pre-kinematic megacrystic biotite granite, (2) post-kinematic hornblende biotite tonalite, (3) migmatite protolith, and (4) the age of migmatization and by inference the age of deformation. Finally, these age were related to how the chronology of the central Santa Fe Range relates to the Proterozoic orogenic history of the southwest.

CHAPTER 3: MIGMATITES

3.1: Terminology

Current migmatite definitions and terminology has been revised by Sawyer (2008) from previous and outdated migmatite terminology (Mehnert, 1968; Ashworth, 1985; Johannes, 1985). As defined by Sawyer (2008), migmatites are medium to high grade metamorphic rocks that have undergone some degree of partial melting (anatexis). Anatectic migmatites are derived from a protolith (pre-existing parent rock) and consist of three basic lithologies: the *paleosome*, the *melanosome* and the *leucosome* (Figure 5). During anatexis the protolith is converted to (1) newly formed material of leucosome and melanosome that are collectively referred to as the *neosome*, and (2) relatively unchanged material termed paleosome. The paleosome is part of a migmatite that was either not affected, or only slightly affected, by anatexis where pre-anatectic structures (e.g. folds, foliations, and layering) are preserved and microstructures are either left unchanged or only slightly coarsened (Sawyer, 2008). The leucosome is the light-colored portion of neosome that is rich in felsic minerals (e.g. quartz and feldspar) and is associated with the melt (silicate liquid) fraction formed from partial melting. The melanosome is the dark-colored portion of neosome that is rich in mafic minerals (e.g. biotite, hornblende, or pyroxene) and is associated with the solid, residual fraction (residuum) of newly formed material that has been extracted from either all, or part of, the melt. It is generally accepted that the solid fraction (residuum) of the melanosome is left in place (in-situ) while the melt fraction of the leucosome is potentially mobile. Segregated melt that remains at the site where the melt has formed is termed *in-situ leucosome* (Sawyer, 2008). A *leucocratic vein or dike* describes melt that has migrated from its source and has been injected into another rock that is still within the region affected by anatexis (Sawyer, 2008). The many syn-kinematic structures that are associated with the development of migmatites are discussed below.

3.2: Syn-kinematic Structures and Morphologies

Syn-kinematic anatectic structures recognized in the Aspen Basin migmatite include in-situ compositional layering, folds, foliations, boudinage features, and leucocratic veins and dikes

(Figure 6). In addition, Metcalf (1990) documented the Aspen Basin migmatite as having a dominant structure which consists of (1) a compositional layering composed of interlayered neosomes and paleosomes (S_1); (2) mica-grainshape foliations (S_1 mica orientation) in paleosomes; and (3) mica-grainshape foliations (biotite orientation) in melanosome selvages (S_2). During this study examples of syn-kinematic anatectic structures were observed in the Aspen Basin migmatite and documented in field photographs. These structures include melt migration features such as (1) in-situ leucosome (Figure 6a), (2) thickened leucosomes in fold noses (Figure 6b, c & d), (3) leucosomes at boudin necks in boudinage features (Figure 6e & f), and (4) leucocratic veins and dikes (Figure 6g & h). Figure 6a illustrates in-situ leucosome or the compositional layering of neosome and paleosome that is the dominant S_1 fabric observed. Most elements in Aspen Basin migmatite outcrops are coplanar and folds exhibited within the compositional layering range from being tight to isoclinal, intrafolial folds, where parasitic folds are also documented as well (Figure 6b, c & d); all of which are prominent throughout the Aspen Basin migmatite unit. Metcalf (1990) also observes mica foliations (S_2) in paleosomes and melanosomes that wrap around fold hinges, and foliations that are coplanar with the axial surface of intrafolial folds that are coplanar with F_2 axial surfaces in refolded folds (where present). Based on these relationships, a composite S_1/S_2 fabric seen at the outcrop scale is considered to be the dominant planar fabric (Metcalf, 1990). Other structural features are boudinage features, commonly referred to as boudins and boudin necks (Figure 6e & f). Discordant leucosomes, or leucocratic veins and dikes, (Figure 6g & h) are also present where anatectic melt has migrated into extensional fractures opened during deformation and crosscut the S_1/S_2 foliation. Metcalf (1990) recognized that the composite S_1/S_2 fabric (D_1 – D_2) defines a map scale F_3 (D_3) fold (Figure 4).

CHAPTER 4: SAMPLE DESCRIPTIONS

4.1: Pre-Kinematic Megacrystic Biotite Granite

The pre-kinematic megacrystic biotite granite unit is medium- to coarse-grained (1 millimeter to 3 centimeters) with hypidiomorphic, inequigranular porphyritic textures (Figure 7a). This unit has isolated mats of aligned mica and co-planar shear bands (≤1 millimeter thick) that define a foliation, and which exhibit dynamic recrystallization textures. The mineral assemblage of the pre-kinematic granite is composed primarily of microcline, plagioclase and quartz with accessory + biotite, + apatite, + magnetite, + zircon, and ± muscovite. Biotite in this unit is estimated to range between 10-15 percent, and alkali feldspar megacrysts are comprised primarily of plagioclase and microcline. The pre-kinematic granite unit exhibits a pervasive S_1 subsolidus foliation that is defined by the alignment of biotite mats, the orientation of plagioclase and microcline megacrysts, and by millimeter-thick ductile shear bands (Metcalf, 1995; Metcalf, 1990).

The megacrystic biotite granite is exposed at both the southeastern and northeastern portions of the Aspen Basin septum. The contact between the megacrystic biotite granite is gradational to the megacrystic granite; however this unit is interlayered with the migmatite unit on a scale of 0.5 to 5 meters (Metcalf, 1995). Field relationships and observations indicate the S_1 foliation in the pre-kinematic megacrystic biotite granite is coplanar with a S_1/S_2 foliation seen in the Aspen Basin migmatites (Figure 7b) (Metcalf, 1990). Discordant leucosomes observed also cross-cut both the S_1/S_2 syn-anatectic fabrics of the migmatites and the S_1 foliation of the pre-kinematic granite (Figure 7b).

4.2: Post-Kinematic Hornblende Biotite Tonalite

The post-kinematic hornblende biotite tonalite unit is medium-grained (1 to 5 millimeters) with hypidiomorphic, inequigranular seriate textures (Figure 7c) and where present, foliations can be defined by the weak alignment of isolated mats of biotite (Metcalf, 1990). The mineral assemblage is primarily comprised of plagioclase, quartz and biotite, with accessory + microcline, + zircon, + hornblende, + sphene, + apatite, ± oxides, and ± chlorite. Plagioclase grains exhibit

some coarse and patchy pericline twinning with an antiperthite texture (Metcalf, 1995). Plagioclase and biotite are generally randomly oriented and therefore the hornblende biotite tonalite unit generally has no internal foliation or mineral alignment; only in narrow centimeter- to meter-scale planar zones does an internal foliation become apparent by a weak alignment of biotite grains (Metcalf, 1995). The hornblende biotite tonalite unit crops out at the southern portion of the Aspen Basin septum and exhibits a sharp contact between the megacrystic biotite granite and migmatitic supracrustal rock units (Figure 7d). The hornblende biotite tonalite unit cross-cuts both the S_1 foliation of the megacrystic biotite granite and the S_1/S_2 foliation of the migmatite units.

4.3: Aspen Basin Migmatite

Aspen Basin migmatite samples exhibit a variance of mineral assemblages and textures between corresponding layers of leucosome, melanosome and paleosome. Paleosome samples are generally fine-grained (0.2 to 1.0 millimeters) with granoblastic-polygonal textures and internal grainshape foliations defined by mica alignment (Metcalf, 1990). Paleosomes are primarily comprised of quartz, biotite and plagioclase, + magnetite, + zircon, + muscovite, ± garnet, ± oxides, and ± chlorite. Leucosome samples are coarse-grained (2 to 20 millimeters) and lack granoblastic-polygonal textures or internal foliations (Figure 7e). Leucosomes are primarily comprised of quartz, plagioclase and muscovite, ± biotite, ± oxides, ± microcline, ± zircon, ± apatite, ± sillimanite, and ± chlorite. Melanosome samples are coarse-grained (1 to 10 millimeters) and display a strong grain shape foliation defined by the alignment of micas and oxides (Figure 7f) (Metcalf, 1990). Melanosomes are primarily comprised of biotite, muscovite and oxides, + zircon, ± garnet, ± sillimanite, ± quartz, ± plagioclase, and ± chlorite. All migmatite samples include chlorite and epidote as secondary alteration products.

Located in the central portion of the Aspen Basin septum, the biotite gneiss unit has a sharp contact between the felsic gneiss unit on the west and east portion of the Aspen Basin septum, that forms the limbs to a large map scale F_3 antiform located at the center of the biotite gneiss unit (Figure 4). As previously stated, dominant textures include a compositional S_1

foliation defined by compositional interlayering of neosomes and paleosomes, and a mica-grainshape foliation that is observed in paleosome and melanosome selvages (Metcalf, 1990). Mica-grainshape foliations are generally observed as wrapping around fold hinges and in the axial surface of fold noses where biotite becomes reoriented and are co-planar with the axial surface of intrafolial folds (Metcalf, 1990). Although rare, there are parasitic folds that have been refolded where biotite grains are coplanar with F_2 axial surfaces. In some outcrops, the compositional S_1 foliation is refolded into tight and isoclinal folds, displaying a composite S_1/S_2 fabric. This composite S_1/S_2 fabric is the dominant planar fabric observed in most outcrops of the biotite gneiss unit.

CHAPTER 5: ANALYTICAL METHODS

Zircon mineral separates were produced from six samples that include a pre-kinematic megacrystic biotite granite (sample 8510-7), a post-kinematic hornblende biotite tonalite (sample 04-01) and four migmatite samples; one set from a contiguous leucosome-melanosome-paleosome triplet (samples 01-02L, 01-02M, 01-02P) and a few additional zircon crystals are from a second melanosome unit (sample 079-3M). Migmatite samples were initially separated using rock saws to cut out and separate paleosome, melanosome and leucosome. Both plutonic units and migmatite samples were crushed using the Chipmunk rock crusher and Bico disc mill pulverizer then sieved to <106μm in preparation for heavy liquid density separation. Magmatic fractions (e.g. magnetite) were removed from each sample with hand magnet. Zircon crystals were obtained from each sample by the method of heavy liquid density separation using methylene iodide (specific gravity of 3.32); where the dense fraction obtained from separation was finally run through a magnetic Frantz separator. Zircon crystals were then hand-picked under a binocular microscope.

Zircon crystals were mounted in epoxy and polished to expose grain interiors then were gold coated and spot analyzed for U-Pb isotopes and Th-U trace element concentrations using standard methods (Ireland and Williams, 2003) on the high-spatial resolution Secondary Ion Mass Spectrometer (SIMS) located at the University of California, Los Angeles (UCLA). Trace element compositions (Th and U) were measured using the UCLA CAMECA ims 1270 ion probe (Schmitt et al., 2003). Geochronologic evaluation of U-Pb isotopic data and Th-U concentrations were carried out using Isoplot 3.6 software (Ludwig, 2008) that runs in Microsoft Excel. Isotopic age calculations were obtained from concordant data sets with statistical data point errors that are given in a 95% confidence interval (2-σ).

Quantitative wavelength dispersive chemical analyses where also collected on Aspen Basin migmatite zircon using the JEOL 8900 Electron Probe Microanalyzer (EPMA) at the University of Nevada, Las Vegas (UNLV) with an analytical spot size of 1μm and a beam current of 20 nanoamps. Natural silicate minerals were used as standards. The study primarily focused on the FeO, CaO, and Al_2O_3 oxides, as these have been interpreted as providing evidence for

hydrothermal alteration in zircon by the interaction between late-stage fluids/melts (Geisler et al, 2007). Standard oxides for Cr_2O_3, FeO, MoO_3, ZrO_2, TiO_2, CaO, Al_2O_3, HfO_2, and SiO_2 were analyzed for leucosome, melanosome and paleosome zircon. The EMPA analytical spots were selected to correspond to previously analyzed SIMS spots.

CHAPTER 6: ZIRCON OCCURRENCE AND MORPHOLOGY

6.1: Plutonic Zircon

Zircon crystals of both the pre-kinematic megacrystic biotite granite and post-kinematic hornblende biotite tonalite units were examined in thin section for crystal habit, location in the sample and general descriptions. Zircon grains in the pre-kinematic megacrystic biotite granite are primarily found as inclusions in both biotite grains and alkali feldspar megacrysts. Some zircon grains are also found at grain boundaries between plagioclase crystals and biotite mats. Megacrystic biotite granite zircons range from small- to medium-sized and are generally subhedral to anhedral, where smaller grains become progressively more stubby and prismatic with rounded edges. Megacrystic biotite granite zircon are light brown in plane polarized light that display high third to fourth order colors in cross polarized light, and most zircon grains in this unit are moderately to highly fractured. Pleochroic halos are commonly found around zircon grains that are included in biotite crystals; however, they are not as distinctive in the megacrystic biotite granite as they are in the migmatitic supracrustal rocks.

Zircon grains in the post-kinematic hornblende biotite tonalite unit are primarily included in biotite grains but are also found as inclusions in some chlorite grains as well. Grains are small-sized and are mostly euhedral, elongate grains with rounded edges. Zircon grains are light tan in plane polarized light and exhibit high second to third order colors in cross polarized light. Zircon exhibit little to no visible fractures and there is no visible evidence of pleochroic halos surrounding grains that are included in biotite or chlorite crystals.

6.2: Migmatite Zircon

Migmatite zircon crystals were examined by (1) cathodoluminescent imagery in grain mounts and (2) optically in thin section for habit, general descriptions and their location within each sample of the Aspen Basin migmatite unit.

Thin section analysis: Leucosome zircon crystals are found within muscovite crystals with some altered halos surrounding zircons, included in quartz and located along muscovite and quartz grain boundaries. The altered halos are often referred to as pleochroic halos, most often

found in biotite, and are thought to be caused by radiation damage. Leucosome zircon is euhedral to subhedral and varies from very elongate (~4:1; length to width) with prismatic habit to shorter (~2:1) crystals with rounded edges. Leucosome zircon grains range from 50-150 micrometers (μm) in size where moderate fractures are observed in larger (≥75μm) crystals. Colors range from clear to light tan in plane-polarized light, and exhibit strong second to third order colors in cross-polarized light. Melanosome zircon is included in quartz, muscovite and biotite crystals, where sharp pleochroic halo boundaries are only noted around zircons located within biotite crystals. Melanosome zircon is euhedral to primarily subhedral and slightly elongate (~3:1) with some prismatic crystals, to less elongate (~2:1) with rounded edges. Melanosome zircon grains range from 50-100μm in size with the primary population being ≤75μm, and are moderately fractured in larger (≥75μm) crystals. Colors range from clear to light tan in plane-polarized light, and exhibit low through high second order to low through moderate third order colors in cross-polarized light. Fractures are not readily apparent in small (≤50μm) crystals from either the leucosome or melanosome samples. Paleosome zircon are located within quartz crystals and are found between biotite-quartz-iron oxide grain boundaries. Paleosome zircon are subhedral to anhedral, generally are not prismatic and less elongate (~2:1) with rounded edges. The majority of the paleosome zircon population is <75μm in size, exhibit high positive relief with no visible fractures, and colors range from clear to light-tan in plane-polarized light, with moderate to high second order colors in cross-polarized light.

Cathodoluminescent analysis: Internal textures of leucosome and melanosome zircon from sample were analyzed in grain mount by cathodoluminescent (CL) surface microscopy to distinguish inherited cores and new growth rims to select spots for Secondary Ion Mass Spectrometry (SIMS) analysis (Figure 8). Leucosome (sample 079-3L, Figure 8a) and melanosome (sample 079-3M, Figure 8b) zircon luminescence is very low, such that inherited cores from new growth could not be distinguished. As seen in Figure 8, images exhibit low luminescence that is interpreted to be a result of high uranium content, paired with radiation damage due to radioactive decay of uranium and thorium series elements leading to severe damage to the crystal structure (metamictization) (Geisler et al., 2007). Featureless grey-

cathodoluminescent images may also be explained by transgressive recrystallization fronts of protolith zircon, such as those observed by Hoskin and Black (2000) (see their Figure 2). Recrystallization fronts are proposed to occur in the solid state, without the need for a fluid-phase interaction between the zircon crystal and melt (Hoskin & Black, 2000; Geisler et al., 2007). Lacking CL imaging as a guide, SIMS analytical spots were selected from zircon centers and rims (tips).

CHAPTER 7: RESULTS

7.1: Secondary Ion Mass Spectrometer (SIMS) Analysis of Zircon

SIMS analytical data and calculated ages are presented in Tables 1 through 3 and Figures 9 through 14. In the tables uncertainties are reported at 1σ but all age uncertainties in the figures and discussed in the text below are given at 2σ.

Plutonic Samples: A total of fourteen spots were analyzed on nine individual zircon grains from the megacrystic biotite granite, sample 8510-7. Results include $^{206}Pb/^{238}U$ ages ranging from 1.346 Ga to 1.705 Ga, $^{207}Pb/^{235}U$ ages ranging from 1.435 Ga to 1.657 Ga and $^{207}Pb/^{206}Pb$ ages ranging from 1.570 Ga to 1.650 Ga (Table 1). A subset of the U-Pb ages plot as concordant (6 of 14) on the concordia diagram and the remainder are only slightly discordant (Figure 10). Uranium concentrations in sample 8510-7 zircon range from 260 ppm to 1,400 ppm; thorium concentrations range from 112 ppm to 594 ppm (Table 1, Figure 9a). Th/U ratios for the pre-kinematic granite range from 0.291 to 0.846 and are within typical ranges for igneous rocks (>0.5) (Hoskin & Schaltegger, 2003). As discussed below, a straight forward age interpretation for the age of the megacrystic biotite granite (sample 8510-7) is ~1.63 Ga.

A total of thirteen spots were analyzed on six individual zircon grains from the hornblende biotite tonalite, sample 04-01. Results include $^{206}Pb/^{238}U$ ages ranging from 1.174 Ga to 1.475 Ga, $^{207}Pb/^{235}U$ ages ranging from 1.222 Ga to 1.446 Ga and $^{207}Pb/^{206}Pb$ ages ranging from 1.261 Ga to 1.428 Ga for the post-kinematic tonalite (Table 2). All but two of the U-Pb ages plot as a single concordant age on the concordia diagram with the remainder being only slightly discordant (Figure 11). Uranium concentrations in sample 04-01 zircon range from 210 ppm to 1,600 ppm; thorium concentrations range from 82 ppm to 469 ppm (Table 2, Figure 9b). With the exception of one outlier, Th/U ratios for the post-kinematic tonalite range from 0.053 to 0.505 and also lie within typical ranges for igneous rocks. As discussed below, a straight forward age interpretation for hornblende biotite tonalite (sample 04-01) is ~1.4 Ga.

Migmatite Samples: Zircon from the four migmatite samples (01-02L, 01-02M, 01-02P, and 079-3M) were analyzed in three groups separated by leucosome, melanosome and paleosome as follows: leucosome (12 from 01-02L), melanosome (7 from 01-02M, 3 from 079-

3M) and paleosome (7 from 01-02P) with a total of forty-four analytical spots on twenty-nine individual zircon grains. Total analyses include twenty-four spots on twelve individual leucosome zircon grains (Table 3a), thirteen spots on ten individual melanosome zircon grains (Table 3b) and seven spots on seven individual paleosome zircon grains (Table 3c).

Leucosome zircon $^{206}Pb/^{238}U$ ages range from 515 Ma to 1.498 Ga, $^{207}Pb/^{235}U$ ages range from 677 Ma to 1.545 Ga and $^{207}Pb/^{206}Pb$ ages range from 1.326 Ga to 1.641 Ga (Table 3a). Leucosome zircon U varies widely from 240 ppm to 9,300 ppm; Th concentrations vary from 3 ppm to 276 ppm. Th/U ratios for leucosome zircon range from 0.004 to 0.110 (Table 3a, Figure 9c). Melanosome zircon $^{206}Pb/^{238}U$ ages range from 1.005 Ga to 1.639 Ga, $^{207}Pb/^{235}U$ ages range from 1.199 Ga to 1.664 Ga and $^{207}Pb/^{206}Pb$ ages range from 1.392 Ga to 1.794 Ga (Table 3b). Melanosome zircon uranium varies from 370 ppm to 2,400 ppm; thorium concentrations vary from 22 ppm to 1,788 ppm. Th/U ratios range from 0.014 to 0.745 (Table 3b, Figure 9c). Paleosome zircon $^{206}Pb/^{238}U$ ages range from 815 Ma to 2.131 Ga, $^{207}Pb/^{235}U$ ages range from 1.002 Ga to 2.075 Ga and 1.410 Ga to 2.020 Ga ($^{207}Pb/^{206}Pb$) (Table 3c). Paleosome zircon uranium range from 230 ppm to 2,900 ppm; thorium concentrations range from 48 ppm to 667 ppm. Th/U ratios range from 0.032 to 0.638 (Table 3c, Figure 9c). In general, migmatite zircon age ranges and Th/U ratios shown have a much greater variation than that seen in zircons from the two plutonic rocks.

7.2: Electron Probe Microanalysis (EPMA) of Migmatite Zircon

Electron microprobe results for migmatite zircon are shown in Table 4 and Figure 15. All EPMA spots that were selected for analysis were chosen from a subset of the SIMS analytical points that yielded a mix of U-Pb isotopic ages and low Th/U values in order to test and document hydrothermal alteration in migmatite zircon. Fourteen spots were analyzed on seven zircon crystals in the leucosome where FeO values range from 0 to 1.05-weight percent (wt%), Al_2O_3 values range from 0 to 1.32 wt% and CaO values range from 0.01 to 1.82 wt%. Three spot counts were analyzed on three zircon crystals in the melanosome where FeO values range from 0.02 to 0.12 wt%, Al_2O_3 values range from 0 to 0.05 wt% and CaO values range from 0.002 to

0.01 wt%. Lastly, five spot counts were analyzed on five zircon crystals in the paleosome, where FeO values range from 0 to 0.1202 wt%, Al_2O_3 values range from 0 to 0.0805 wt% and CaO values range from 0.01 to 0.25 wt%.

CHAPTER 8: INTERPRETATION OF AGES

8.1: Plutonic Ages

The $^{207}Pb/^{206}Pb$ weighted average age of all zircon analyses for the pre-kinematic granite is 1622 ± 12 Ma with a mean standard weighted deviation (MSWD) of 1.6 (Figure 10a). A U-Pb concordia plot of all zircon analyses, some of which are slightly discordant, yielded an upper intercept age of 1631 ± 13 Ma (MSWD = 0.97, Figure 10b). Removal of discordant analyses yielded a concordant age of 1633 ± 12Ma (MSWD = 1.04, Figure 10c). The Th/U ratios (0.291 – 0.846) (Table 1) for pre-kinematic granite zircon plot within normal ranges for igneous rocks which is typically ≥0.5 (Hoskin & Schaltegger, 2003). An age of 1633 ± 12 Ma is accepted for crystallization of pre-kinematic megacrystic biotite granite.

The $^{207}Pb/^{206}Pb$ weighted average age of all zircon analyses for the post-kinematic tonalite yielded a mean age of 1382 ± 21 Ma (MSWD = 2.4, Figure 11a). All but two zircon analyses cluster on the U-Pb concordia (Figure 11b), removal of those two analyses yielded a concordant age of 1395 ± 7 Ma (MSWD = 0.73, Figure 11c). The post-kinematic hornblende biotite tonalite zircon yielded Th/U ratios in the range normal for igneous rocks (0.362 – 0.505) with the exception of one outlier (0.053) (Table 2). An age of 1395 ± 7 Ma is accepted for crystallization of the post-kinematic hornblende biotite tonalite.

8.2: Migmatite Ages

The evaluation of migmatite ages begins with the combined leucosome-melanosome-paleosome data set. The $^{207}Pb/^{206}Pb$ relative probability (Figure 12a) and weighted average (Figure 12b) of ages for the combined migmatite data set shows a broad continuum of ages from 2.1 Ga to 1.3 Ga; three clear peaks are seen on the relative probability plot at about 1.8 Ga, 1.6 Ga and 1.4 Ga (Figure 12a); these peaks correlate with ages common to Proterozoic crust of the southwest (Figure 2). However, ages that fall between peaks at 1.6 Ga and 1.4 Ga are suspect because the interval between 1.6 Ga and 1.5 Ga is thought to represent a time of crustal stability with few magmatic or metamorphic ages reported from North America (Figure 2; Karlstrom et al 2004). Hoskin and Black (2000) reported similar 'mixed' U-Pb isotope zircon ages in

Paleoproterozoic high-grade metagranitoids from Queensland, Australia. Using zircon trace element chemistry, including highly variable Th/U ratios, Hoskin and Black (2000) attributed these mixed ages to a process of solid-state recrystallization during high-grade metamorphism. Following Hoskin and Black (2000), Th/U ratios were used to 'screen' the Aspen Basin migmatite zircon data set.

Migmatite Th/U ratios vary significantly from igneous-like values to both very low Th and to elevated U concentrations (Figure 9c). Re-plotting the $^{207}Pb/^{206}Pb$ ages using only the fourteen zircon analyses with Th/U ratios >0.1 yielded two distinct populations (Figure 13), population 1 with a weighted average at 1634 ± 16 Ma (MSWD = 0.41, n = 6) and population 2 with a weighted average at 1398 ± 17 Ma (MSWD = 0.88, n = 5); three additional analyses have $^{207}Pb/^{206}Pb$ ages of 1791 ± 25 Ma. A U-Pb concordia plot of population 1 (Figure 14a) yielded an upper intercept age of 1635 ± 17 Ma (MSWD = 1.18), very close to the $^{207}Pb/^{206}Pb$ age. The U-Pb concordia plot for population 2 (Figure 14b) is concordant and yielded an age of 1386 ± 28 Ma (MSWD = 0.022), also very close to the $^{207}Pb/^{206}Pb$ age. Both older ages of 1791 ± 25 Ma and 1636 ± 16 Ma are accepted as geologically meaningful ages for zircon inheritance in the migmatite protolith. The younger age of 1398 ± 15 Ma is accepted as the age of migmatization and specifically the crystallization of anatectic melts, and dates a portion of the metamorphic and retrograde P-T-time path.

CHAPTER 9: EVIDENCE OF ZIRCON RECRYSTALLIZATION IN ASPEN BASIN MIGMATITE

Background: A lack of internal textures is a common feature seen in zircon that has been modified by recrystallization of protolith zircon (Hoskin & Black, 2000); recrystallization may not always proceed to completion and often leaves zircon crystals that display areas where primary textures (zoning) has been destroyed. As seen in cathodoluminescence imagery, Hoskin and Black (2000) document either modification or a complete loss of primary igneous zoning and internal textures, where areas of recrystallization and preservation yield contrasting luminescence from low to high respectively. Hoskin and Black (2000) attributed such areas of low luminescence to transgressive recrystallization fronts that provide evidence for solid-state recrystallization. Observations of dark-grey areas in cathodoluminescence images are seen adjacent to recrystallized areas and are hypothesized as being trace element-enriched selvedges that precede transgressive recrystallization that are termed *recrystallization fronts*. Hoskin and Black (2000) also documented a large spread in apparent ages ('mixed' ages) of U-Pb isotopic data from these recrystallized areas. The age spread is interpreted as being an incomplete re-setting of U-Pb isotopic compositions due to varying degrees of partial recrystallization. As recrystallization proceeds through the zircon crystal, there is also a differential expulsion of Th and U that results in a progressive change to the Th/U ratio (Hoskin & Black, 2000), where it is observed that uranium is most abundant in areas affected by recrystallization. The change in Th/U ratio to less than 0.1 is noted for recrystallized, metamorphic zircon. Trace elements (e.g. Th and U) in protolith zircon become purged during recrystallization; becoming enriched in the area of the recrystallization front but depleted in the areas of complete recrystallization (Hoskin and Black, 2000). It is important to note that recrystallization is not always efficient and often will leave a 'memory' of the protolith trace element and isotopic composition (Hoskin & Black, 2000) and therefore establishes a correlation between the apparent age and Th/U ratio preserved in the zircon crystals. Because trace elements become mobile during such processes, Th/U ratios with very low values have been documented as being indicative of recrystallization and hydrothermal alteration.

It was concluded that Hoskin and Black's (2000) zircon samples recrystallized in the solid-state as trace element compositions are generally lower in recrystallized areas compared to their protolith counterparts. However, in most crystals from one sample (95836597, Junction Creek) Hoskin and Black (2000) do observe an enrichment of trace elements that are retained in secondary structures and are associated with trace element-enriched recrystallization fronts that are sites for migration of trace elements and a defect-rich boundary that precedes recrystallization through the crystal. Hoskin and Black (2000) noted that even low concentrations of 'impurity' elements in the zircon lattice will generate large amounts of structural stress to the crystal, and recrystallization is thermoactivated where stress can be reduced by the expulsion of large-radius trace elements that are bound in the lattice. Therefore, Hoskin and Black (2000) propose recrystallization operates through a mechanism of grain-boundary and defect migration (and not through diffusion) that is initiated in areas of high lattice strain where a trace element/defect-enriched recrystallization front migrates through the crystal. They attribute this thermoactivation of zircon recrystallization and trace element re-ordering to the presence of inter-granular fluids that are deemed 'kinetically' crucial in providing a considerably larger thermal conductivity for the expulsion of trace elements that reduces stress to the crystal lattice.

In another study, Geisler et al. (2007) discussed recrystallization of zircon by a coupled dissolution-reprecipitation mechanism that operates in the presence of a fluid or melt. In this process, trace elements are transferred between melt/fluid and solid crystal interfaces. Geisler et al. (2007) reported the importance of self-irradiation damage (metamictization) as representing sites where enhanced chemical transport is possible within the zircon crystal. Experimental studies by Geisler et al. (2003a) reported an increase in cathodoluminescence intensity and interpreted this to reflect structural recovery of radiation-damaged zircon, where recovery is greatly enhanced in the presence of water. During recrystallization of amorphous zircon, strain is released from the crystal by fracturing and by producing a porous structure in the crystal that provides pathways allowing for fast chemical exchange between an inward-moving reaction front (recrystallization front) and fluid that is in contact with the crystal (Geisler et al., 2007). This has been documented in experimentally altered areas of zircon crystals where high concentrations of

solvent cations (e.g. Ca^{2+}, Fe^{2+}, and Al^{3+}) were incorporated into reacted domains (Geisler et al., 2003a) and where there was a reported loss of minor and trace elements (e.g. Th). Similar to Hoskin and Black (2000), Geisler et al. (2007) reported these experimentally reacted domains retain a memory of their U-Pb isotopic compositions that results in discordant ages, interpreted as being the result of a moving recrystallization front throughout the crystal structure. The driving force for the coupled dissolution-reprecipitation process is the solubility difference exhibited between a solid solution-aqueous solution system; this is maintained by the formation of porosity that allows for chemical exchange between the zircon crystal and fluid/melt (Geisler et al., 2007).

Both Hoskin and Black (2000) and Geisler et al. (2007) underscore the importance of recognizing recrystallization processes in altered zircon for correct interpretation of apparent ages attained from the U-Pb isotopic system. Their studies attribute observed zircon recrystallization to the presence of a fluid/melt and can document recrystallized zircon by the presence of low Th/U ratios. Other studies by Harley et al. (2007), Carson et al. (2002a), Harley et al. (2001), and Vavra et al. (1999) also document metamorphic zircon with very low (<0.02) Th/U values as being indicative of late-stage melt/fluid interaction and hydrothermal alteration.

***Recrystallization of Aspen Basin zircon*:** A Th/U plot for the entire Aspen Basin migmatite zircon data set is shown in Figure 9c; leucosome, melanosome and paleosome, and are color-coded for distinction between lithologies. Paleosome analyses primarily plot between Th/U = 1.0 – 0.1, in and around the typical range for igneous rocks. A total of seven spots were analyzed from paleosome zircon; five spots lie above Th/U = 0.1, the remaining two analyses plot between Th/U = 0.1 – 0.01. A total of thirteen spots were analyzed from melanosome zircon; seven spots plot above Th/U = 0.1, six spot analyses plot between Th/U = 0.1 – 0.01. A total of twenty-four spots were analyzed from leucosome zircon; two spots plot above Th/U = 0.1, fourteen spots plot between Th/U = 0.1 – 0.01, eight spots plot below Th/U = 0.01. Many of the leucosome zircon analyses have very high U values (>5000 ppm). Low Th/U values and high uranium concentrations are most common in leucosome then melanosome and least in paleosome. It is interpreted that fluid and/or melt interaction is highest in leucosome and

becomes progressively less in melanosome and paleosome respectively; perhaps during melt crystallization in the leucosome fluid is released and promotes recrystallization of zircon crystals.

Additional tests for hydrothermal alteration in metamorphic zircon was demonstrated by Geisler et al. (2007), where coupled dissolution-reprecipitation from late-stage fluid/melt interactions incorporated soluble cations (e.g. Fe^{2+}, Al^{3+}, Ca^{2+}) into the structure of recrystallized areas of the zircon crystal. Plots of FeO, Al_2O_3, and CaO versus U concentrations (ppm) for Aspen Basin migmatite zircon (Figure 15) reveal analyses with low Th/U ratios also having higher concentrations of these soluble cations. As illustrated in Figure 15, the primary increase of these soluble cations occurs within leucosome zircon. This analysis supports the notion that Aspen Basin migmatite zircon has undergone hydrothermal alteration by late-stage fluid interaction during anatexis (~1.4 Ga), and generally is found to correspond to Th/U values that are less than 0.1. This provides justification for removing U-Pb analyses that yield Th/U values less than 0.1 in migmatite zircon as previously discussed for age interpretations. Upon removal of such analyses $^{207}Pb/^{206}Pb$ weighted averages, relative probability counts, and U-Pb concordia diagrams for Aspen Basin zircon now yield interpretable geologic ages.

CHAPTER 10: DISCUSSION

10.1: Zircon Behavior during Anatexis at Aspen Basin

Experimental studies performed by Harrison & Watson (1983) and Watson & Harrison (1983) suggest that the rate and extent of zircon dissolution and growth can be influenced by temperature and the composition and water content of the melt. In typical crustal-derived melts (H_2O > 2 wt%), Watson & Harrison (1983) demonstrated zirconium (Zr) concentration in the melt (C_{Zr}(melt)) is a function of both temperature (T) and melt composition (M) which provided the experimentally derived equation for zircon saturation, equation (1): $C_{Zr}(melt) = C_{Zr}(zircon) \cdot \exp[3.80 + 0.85(M-1) – 12900/T]$, where C_{Zr} (zircon) is ~50% for stoichiometric zircon, M is the cation ratio (Na + K + 2Ca)/(Al/Si), and T is the absolute temperature (Nemchin et al., 2001). Potential complications between zircon-melt interactions were recognized in two chemically distinct leucosome types (Watt & Harley, 1993; Watt et al., 1996; Bea & Montero, 1999). The first type is slightly zircon-undersaturated and the second type is zircon-oversaturated, the latter representing leucosome with inherited zircon.

An understanding of the solubility of zircon in silicate melts allows for a discussion of the behavior of zircon during 1.4 Ga anatexis. Harley et al. (2007) presented a schematic diagram of a temperature (T)-time (t) path that illustrates the behavior of zircon crystals during a hypothetical high-T anatectic event. A version of this graph has been modified to reconstruct the behavior of zircon crystals in the Aspen Basin migmatite during anatexis (Figure 16).

On the prograde metamorphic path the water-saturated solidus marks the onset of partial melting (anatexis) of the migmatite protolith at 1.4 Ga, where dissolution of protolith (inherited) zircon begins in newly formed melt ([a] in Figure 16). At this stage the melt fraction was relatively low and zircon undersaturated, but progressively increased as temperatures increased, allowing for additional zircon dissolution ([b] in Figure 16). For a given melt composition and maximum T, and with a significant abundance of inherited zircon, the melt can become zircon saturated resulting in entrained inherited zircon crystals ([c] in Figure 16). This appears to be the case for the Aspen Basin migmatites which preserve 1.63 Ga and older zircon. In the Aspen Basin migmatite, the thermal peak never quite reached temperatures that exceeded those which

initiated dehydration reactions, such as those involving biotite (Metcalf, 1990) suggesting these were wet melts ([c] in Figure 16). Upon cooling zircon began to crystallize ([d] in Figure 16) as new growth rims (~1.4 Ga) on protolith zircon cores (≥ 1.63 Ga). During the final stages of crystallization at or near the solidus, late stage fluid/melt reactions with zircon occurred in the solid-state and resulted in hydrothermally altered zircon crystals ([e] in Figure 16), as evidenced by reported low Th/U ratios and increased U and soluble cation concentrations.

Hydrothermal alteration resulted in a chemical re-equilibration of crystalline zircon (both 1.4 Ga and ≥1.63 Ga zircon), during which aqueous fluid or melt interacted with zircon by a coupled dissolution-reprecipitation process similar to that discussed by Geisler et al., (2007). During late stage fluid/melt interactions ([e] in Figure 16) Aspen Basin zircon crystals gained significant amounts of solvent cations (e.g. Ca^{2+}, Fe^{2+}, Al^{3+}), lost Th and redistributed U. When late stage fluid and melt interactions are coupled with self-irradiation damage, the stability of the U-Pb isotopic system in zircon reveals isotopic discordance that often becomes dramatic once a threshold for uranium content has been reached (Williams, 1992). It has been concluded that hydrothermal recrystallization of Aspen Basin migmatite zircon was incomplete with inward diffusion of soluble cations via a recrystallization front, with zircon crystals retaining high concentrations of soluble cations and uranium. These portions of the zircon crystals remained open to isotopic exchange since 1.4 Ga, enhanced by accumulated radiation damage in high U zones, and resulted in “mixed” ages and U-Pb isotopic discordance (Figure 12). Finally, poor quality CL images are likely a result of incomplete recrystallization and self-irradiation damage.

10.2: Implications for Precambrian Geology

The most critical concern regarding the Proterozoic tectonic history of the New Mexican region is the age and timing of plutonism, metamorphism and deformation. Uranium-Pb isotopic analyses yielded a crystallization age for the megacrystic biotite granite at 1633 ± 12 Ma (Figure 10). This correlates with later stages of the Mazatzal orogeny (1.67 Ga to 1.65 Ga) where peak deformation was said to occur at approximately 1.65 Ga, affecting both Yavapai and Mazatzal crust (Karlstrom et al., 2004; Bauer et al., 1993; Karlstrom & Bowring, 1993). Petrographic

evidence of observed solid-state deformation features (e.g. ductile shear bands and the orientation of biotite mats and feldspar megacrysts) in the megacrystic biotite granite suggest deformation fabrics are not older than the crystallization age at 1633 ± 12 Ma in the Santa Fe Range. Field relationships (Figure 7b) indicate the S_1 deformation fabric in the megacrystic biotite granite is parallel to the composite S_1/S_2 foliations in the Aspen Basin migmatite and suggests deformation was syn-kinematic with anatexis and migmatite formation at ~1.4 Ga.

Zircon inheritance from the Aspen Basin migmatite records $^{207}Pb/^{206}Pb$ ages at ~2100 Ma, 1791 ± 25 Ma and 1636 ± 16 Ma (Figures 13 & 14). Multiple inherited age generations suggest the migmatite protolith was most likely metasedimentary in origin rather than from an igneous or volcanic source, as sedimentary rocks generally incorporate inherited zircon grains during their formation. Secondly, the migmatite protolith cannot be older than the youngest recorded age of zircon inheritance; therefore the age of the migmatite protolith is no older than 1636 ± 16 Ma. Statistically the migmatite protolith age is indistinguishable from the age of the megacrystic biotite granite; therefore emplacement of the megacrystic biotite granite and migmatite protolith was synchronous. Both the megacrystic biotite granite and the Aspen Basin migmatite protolith represent Mazatzal age crust (Figures 1 & 3).

Deformation features observed in Aspen Basin neosome and paleosome (e.g. compositional layering and mica-grain shape foliations) suggest anatexis and migmatization was contemporaneous with deformation. The age of new growth zircon formed during syn-kinematic anatexis is 1398 ± 15 Ma and thus records the age of migmatization, anatexis and leucosome crystallization in the Aspen Basin migmatite. Thus the Aspen Basin migmatite records both metamorphism and deformation at ~1.4 Ga; this provides additional evidence and documentation of intense metamorphism and deformation at 1.4 Ga as suggested by Bauer et al. (1993), Bishop (1997) and Wingsted (1997) and suggests an orogenic event occurred at ~1.4 Ga.

The crystallization age for the hornblende biotite tonalite at 1395 ± 7 Ma is statistically the same age as that of new growth zircon in the Aspen Basin migmatite; thus mafic magmatism (tonalite crystallization) was broadly synchronous with migmatization. This suggests mafic magmatism could have potentially provided the heat source that drove anatexis at ~1.4 Ga.

Some models (Karlstrom et al., 2004) suggest that crustal underplating of mafic magma was the driver for lower crustal partial melting that generated wide-spread 1.4 Ga granitic (A-type) magmatism. Few ~1.4 Ga ages have been reported for mafic rocks in the southwest; the recognition of ~1.4 Ga mafic magmatism in the Santa Fe Range provides support for this model.

CHAPTER 11: SUMMARY AND CONCLUSIONS

Important conclusions regarding zircon behavior during anatexis, migmatite formation, metamorphism, deformation and tectonism in the Santa Fe range, NM and southwest region are as follows:

1) Chemical evidence from migmatite zircon (decrease in Th/U values and increase of soluble cation concentrations) suggests interaction of anatectic melt and/or hydrothermal fluids that resulted in some degree of chemical alteration during the formation of zircon in the neosome; particularly from the release of water during leucosome crystallization. This suggests neosome zircon experienced chemical alterations from anatectic melts and late-stage hydrothermal fluids in the Aspen Basin migmatite.
2) Pre-kinematic granite crystallization and emplacement occurred at 1633 ± 12 Ma, being broadly synchronous with the late-stage Mazatzal deformation at 1.67 Ga to 1.65 Ga.
3) Aspen Basin migmatite zircon records multiple ages of inheritance at ~2100 Ma, 1791 ± 25 Ma and 1636 ± 16 Ma. Multiple inherited ages suggest migmatite protolith was metasedimentary in origin. Migmatite protolith age is no older than 1636 ± 16 Ma and is synchronous with pre-kinematic granite emplacement.
4) Migmatite new growth zircon in neosome records the age of migmatization, anatexis and leucosome crystallization at 1398 ± 15 Ma. Syn-kinematic structures observed in the migmatite also documents deformation at ~1.4 Ga and therefore record an orogenic event at ~1.4 Ga.
5) Post-kinematic tonalite zircon records a crystallization age at 1395 ± 7 Ma, where migmatite new growth zircon is synchronous with tonalite emplacement.
6) Tonalite emplacement could have provided the heat source that drove anatexis and migmatite formation, and also documents the importance of mafic magmatism and tectonism at ~1.4 Ga.

Geochronologic and petrographic studies of three lithologic units sampled in the Santa Fe range, northern New Mexico, records evidence for metamorphism and deformation associated with the Mazatzal orogeny at ~1.6 Ga and provides additional support for synchronous mafic magmatism,

metamorphism and deformation at ~1.4 Ga in the southwest region. This study also underscores the importance in understanding zircon behavior during anatexis and migmatite formation, as understanding factors and processes of zircon behavior and migmatite formation are necessary to distinguish and interpret correct U-Pb isotopic ages in migmatite zircon.

Table 1. Analytical data of pre-kinematic megacrystic biotite granite (sample 8510-7) zircon by Secondary Ion Mass Spectrometry (SIMS).

Sample ID	$^{206}Pb/^{238}U$ age	age error (1σ)	$^{207}Pb/^{235}U$ age	age error (1σ)	$^{207}Pb/^{206}Pb$ age	age error (1σ)		$^{207}Pb/^{235}U$	1σ error	$^{206}PB/^{238}U$	1σ error	rho	$^{207}Pb/^{206}Pb$	1σ error	$^{204}Pb/^{206}Pb$	1σ error	Th/U	U ppm	Th ppm
8510-7-01r	1439	52	1498	35	1584	40	97.1	3.374	0.152	0.25	0.0101	0.88	0.09789	0.00207	0.00156	0.00010	0.539	470	253
8510-7-02c	1677	57	1649	32	1614	18	99.8	4.073	0.158	0.297	0.0115	0.97	0.09946	0.00097	0.00011	0.00003	0.846	260	220
8510-7-02r	1529	58	1570	36	1625	19	99.4	3.692	0.164	0.2677	0.0114	0.97	0.1	0.001	0.00031	0.00005	0.373	350	131
8510-7-03c	1346	42	1435	28	1570	19	98.6	3.111	0.111	0.2322	0.0081	0.96	0.09715	0.001	0.00073	0.00006	0.308	1100	338
8510-7-03r	1366	41	1462	27	1604	20	98.1	3.219	0.114	0.2361	0.0079	0.95	0.09891	0.00105	0.00103	0.00006	0.388	820	318
8510-7-04c	1705	58	1656	33	1594	20	99.3	4.108	0.164	0.3028	0.0118	0.96	0.09839	0.00104	0.00035	0.00006	0.311	540	168
8510-7-04r	1563	51	1588	29	1622	20	99.4	3.778	0.135	0.2743	0.0101	0.96	0.09987	0.00105	0.00031	0.00005	0.291	440	128
8510-7-05c	1522	51	1549	34	1586	35	98.1	3.597	0.153	0.2662	0.01	0.90	0.098	0.00182	0.00103	0.00010	0.432	260	112
8510-7-05r	1560	59	1589	37	1628	21	99.4	3.784	0.173	0.2738	0.0117	0.97	0.1002	0.0011	0.00033	0.00006	0.450	300	135
8510-7-06c	1512	52	1560	31	1624	10	99.6	3.646	0.141	0.2644	0.0101	0.99	0.1	0.0005	0.00024	0.00003	0.424	1400	594
8510-7-06r	1622	65	1635	38	1650	16	98.7	4.002	0.188	0.2862	0.0131	0.98	0.1014	0.0008	0.00070	0.00005	0.423	880	372
8510-7-07r	1658	52	1652	29	1645	10	99.7	4.091	0.146	0.2933	0.0104	0.99	0.1011	0.0005	0.00016	0.00003	0.430	690	297
8510-7-08c	1624	60	1626	43	1629	53	95.1	3.961	0.212	0.2866	0.012	0.85	0.1002	0.0028	0.00260	0.00018	0.355	320	114
8510-7-09c	1686	62	1657	34	1620	11	99.8	4.111	0.17	0.2989	0.0124	0.99	0.09976	0.00057	0.00013	0.00003	0.367	820	301

Table 2. Analytical data of post-kinematic hornblende biotite tonalite (sample 04-01) zircon by Secondary Ion Mass Spectrometry (SIMS).

Sample ID	$^{206}Pb/^{238}U$ age	age error (1σ)	$^{207}Pb/^{235}U$ age	age error (1σ)	$^{207}Pb/^{206}Pb$ age	age error (1σ)		$^{207}Pb/^{235}U$	1σ error	$^{206}PB/^{238}U$	1σ error	rho	$^{207}Pb/^{206}Pb$	1σ error	$^{204}Pb/^{206}Pb$	1σ error	Th/U	U ppm	Th ppm
04-01-01r	1438	63	1415	38	1381	23	99.5	3.029	0.15	0.2499	0.0123	0.97	0.08791	0.00106	0.00025	0.00007	0.444	220	98
04-01-02c	1399	51	1393	31	1385	23	99.8	2.945	0.121	0.2424	0.0097	0.96	0.08811	0.00107	0.00009	0.00004	0.401	230	92
04-01-02r	1366	50	1381	32	1405	20	99.7	2.898	0.122	0.236	0.0095	0.97	0.08905	0.00094	0.00019	0.00005	0.501	330	165
04-01-03c	1174	39	1261	29	1414	29	97.7	2.464	0.098	0.1997	0.0073	0.92	0.08946	0.00137	0.00120	0.00008	0.426	1100	469
04-01-03r	1200	39	1222	34	1261	59	95.7	2.332	0.111	0.2047	0.0073	0.77	0.08265	0.00251	0.00230	0.00015	0.505	440	222
04-01-04c	1301	41	1310	26	1325	16	99.5	2.633	0.095	0.2236	0.0077	0.97	0.08543	0.00072	0.00026	0.00004	0.053	1600	84
04-01-04r	1381	49	1379	31	1377	19	99.4	2.889	0.118	0.2388	0.0093	0.97	0.08773	0.00087	0.00030	0.00004	0.377	490	185
04-01-05c	1475	64	1435	44	1377	39	99.6	3.11	0.176	0.2571	0.0124	0.94	0.08774	0.00176	0.00020	0.00009	0.430	210	90
04-01-05r	1463	50	1446	32	1419	22	99.7	3.153	0.132	0.2549	0.0098	0.96	0.08971	0.00105	0.00016	0.00005	0.362	510	185
04-01-05rr	1386	53	1403	33	1428	19	99.7	2.981	0.128	0.2399	0.0102	0.97	0.09012	0.00088	0.00015	0.00004	0.375	490	184
04-01-06c	1432	50	1410	32	1378	33	99.6	3.011	0.127	0.2488	0.0097	0.91	0.08779	0.00153	0.00021	0.00006	0.371	220	82
04-01-06r	1404	59	1386	34	1359	26	99.7	2.916	0.13	0.2433	0.0113	0.96	0.08693	0.00116	0.00018	0.00005	0.503	230	116
04-01-06rr	1447	53	1411	34	1356	24	99.5	3.013	0.135	0.2517	0.0104	0.96	0.08681	0.00108	0.00029	0.00006	0.435	270	117

Table 3a. Analytical data of Aspen Basin migmatite leucosome (sample 01-02L) zircon by Secondary Ion Mass Spectrometer (SIMS).

Sample ID	$^{206}Pb/^{238}U$ age	age error (1σ)	$^{207}Pb/^{235}U$ age	age error (1σ)	$^{207}Pb/^{206}Pb$ age	age error (1σ)		$^{207}Pb/^{235}U$	1σ error	$^{206}PB/^{238}U$	1σ error	rho	$^{207}Pb/^{206}Pb$	1σ error	$^{204}Pb/^{206}Pb$	1σ error	U/Th	U ppm	Th ppm
01-02Lb_S1	1397	18	1389	12	1378	19	99.4	2.927	0.048	0.2419	0.0035	0.79	0.08777	0.00088	0.00033	0.00004	0.004	670	3
01-02Lb_S3	1382	15	1393	10	1409	16	99.4	2.941	0.039	0.2391	0.003	0.80	0.08921	0.00072	0.00033	0.00004	0.004	690	3
01-02Lb_S4	1066	50	1164	38	1351	97	96.1	2.148	0.117	0.1799	0.0091	0.55	0.08659	0.00433	0.00207	0.00027	0.003	1200	4
01-02Lb-01c	1018	32	1167	26	1456	31	97.3	2.156	0.081	0.171	0.0058	0.90	0.09144	0.0015	0.00142	0.00009	0.025	770	19
01-02Lb-01r	542	15	785	19	1556	38	90.0	1.166	0.041	0.08773	0.0025	0.82	0.09641	0.00193	0.00528	0.00009	0.005	5400	28
01-02Lb-02c	1097	35	1238	30	1493	47	94.4	2.385	0.099	0.1855	0.0065	0.80	0.09327	0.00232	0.00299	0.00013	0.010	730	7
01-02Lb-02r	1458	46	1518	28	1602	13	98.3	3.458	0.122	0.2538	0.0089	0.98	0.09882	0.00068	0.00090	0.00004	0.003	1700	5
01-02Lb-03c	1449	43	1516	28	1610	20	94.9	3.449	0.12	0.252	0.0084	0.95	0.09924	0.00104	0.00273	0.00006	0.029	2300	68
01-02Lb-03c	1408	43	1416	27	1428	22	98.1	3.034	0.108	0.2441	0.0083	0.95	0.09014	0.00104	0.00098	0.00006	0.012	840	10
01-02Lb-03r	1408	43	1416	27	1428	22	98.1	3.034	0.108	0.2441	0.0083	0.95	0.09014	0.00104	0.00098	0.00006	0.012	840	10
01-02Lb-04c	1372	41	1464	27	1600	20	97.7	3.229	0.112	0.2372	0.0079	0.95	0.0987	0.00106	0.00120	0.00006	0.005	1100	6
01-02Lb-04cc	956	26	1154	23	1547	27	95.7	2.116	0.07	0.1599	0.0046	0.90	0.09596	0.00136	0.00228	0.00008	0.010	2900	29
01-02Lb-04r	579	15	835	31	1595	82	77.5	1.276	0.069	0.09402	0.0025	0.59	0.09844	0.0043	0.01193	0.00018	0.008	3400	29
01-02Lb-04rr	1498	45	1545	28	1611	22	96.9	3.581	0.127	0.2616	0.0089	0.94	0.09929	0.00117	0.00165	0.00007	0.004	1100	4
01-02Lb-05c	515	16	703	18	1363	24	96.1	0.9989	0.0344	0.08317	0.00262	0.93	0.08711	0.00109	0.00207	0.00005	0.020	9300	185
01-02Lb-06c	1048	31	1230	25	1565	28	85.0	2.357	0.083	0.1765	0.0056	0.91	0.09686	0.00142	0.00798	0.00008	0.025	6000	151
01-02Lb-06r	1200	35	1357	28	1612	36	89.1	2.804	0.106	0.2047	0.0065	0.86	0.09936	0.00191	0.00579	0.00008	0.036	3000	108
01-02Lb-07c	1398	42	1497	29	1641	29	98.6	3.37	0.126	0.2422	0.0082	0.91	0.1009	0.0016	0.00077	0.00010	0.528	240	127
01-02Lb-07r	648	17	871	32	1489	81	91.1	1.358	0.074	0.1058	0.003	0.64	0.09307	0.00396	0.00473	0.00024	0.110	490	54
01-02Lb-08c	894	27	1099	24	1533	22	95.0	1.953	0.068	0.1487	0.0048	0.94	0.09527	0.0011	0.00263	0.00007	0.046	2500	116
01-02Lb-08r	701	25	924	29	1503	52	86.6	1.484	0.071	0.1148	0.0042	0.82	0.09374	0.00259	0.00712	0.00016	0.022	3500	77
01-02Lb-09c	469	13	677	32	1451	103	86.8	0.9486	0.0607	0.07544	0.00216	0.54	0.0912	0.00495	0.00698	0.00016	0.063	4400	276
01-02Lb-09r	809	23	1044	30	1575	64	94.0	1.796	0.083	0.1338	0.004	0.67	0.09738	0.00335	0.00316	0.00010	0.057	3000	172
01-02Lb-5r	597	17	774	18	1326	27	93.3	1.144	0.039	0.09706	0.00293	0.92	0.08546	0.00117	0.00355	0.00007	0.017	8500	143

Table 3b. Analytical data of Aspen Basin migmatite melanosome (sample 01-02M) zircon by Secondary Ion Mass Spectrometer (SIMS).

Sample ID	$^{206}Pb/^{238}U$ age	age error (1σ)	$^{207}Pb/^{235}U$ age	age error (1σ)	$^{207}Pb/^{206}Pb$ age	age error (1σ)		$^{207}Pb/^{235}U$	1σ error	$^{206}PB/^{238}U$	1σ error	rho	$^{207}Pb/^{206}Pb$	1σ error	$^{204}Pb/^{206}Pb$	1σ error	U/Th	U ppm	Th ppm
01-02Ma-01r	1633	49	1631	30	1628	20	98.7	3.984	0.145	0.2883	0.0099	0.95	0.1002	0.0011	0.00068	0.00005	0.543	730	397
01-02Ma-4int	1639	53	1610	31	1574	22	98.9	3.885	0.151	0.2894	0.0106	0.96	0.09735	0.00112	0.00057	0.00006	0.068	710	48
01-02Ma-5int	1005	30	1199	24	1566	16	98.7	2.256	0.077	0.1687	0.0055	0.97	0.09696	0.00081	0.00067	0.00004	0.074	2000	148
01-02Mb_S1	1374	18	1379	11	1386	14	99.6	2.888	0.04	0.2376	0.0034	0.86	0.08814	0.00065	0.00020	0.00003	0.372	710	264
01-02Mb_S31a	1539	20	1486	11	1412	13	99.8	3.321	0.046	0.2696	0.0039	0.88	0.08934	0.00062	0.00011	0.00002	0.361	680	245
01-02Mb-03c	1435	49	1417	29	1392	12	99.7	3.039	0.116	0.2492	0.0094	0.99	0.08844	0.00057	0.00017	0.00003	0.481	550	265
01-02Mb-07c	1119	34	1278	25	1557	23	98.5	2.521	0.088	0.1896	0.0062	0.94	0.09645	0.00117	0.00079	0.00006	0.041	820	34
01-02Mb-12c	1299	41	1379	26	1505	8	99.6	2.89	0.1	0.2233	0.0077	0.99	0.09387	0.00039	0.00021	0.00002	0.060	1600	96
079-3M-02	1413	11	1570	11	1788	21	98.6	3.695	0.05	0.2451	0.0021	0.55	0.1093	0.0013	0.00076	0.00007	0.745	2400	1788
079-3M-02a	1563	15	1664	12	1794	15	99.1	4.15	0.062	0.2744	0.003	0.85	0.1097	0.0009	0.00048	0.00006	0.607	1400	849
079-3M-03a	1522	19	1525	12	1529	21	98.6	3.491	0.055	0.2664	0.0038	0.72	0.09506	0.00106	0.00072	0.00006	0.087	730	64
079-3M-03b	1303	18	1410	13	1577	25	98.9	3.011	0.05	0.224	0.0034	0.64	0.09748	0.00132	0.00060	0.00006	0.014	1600	22
079-3M-05b	1241	31	1419	20	1699	40	97.4	3.047	0.081	0.2122	0.0059	0.68	0.1041	0.0023	0.00137	0.00012	0.441	370	163

Table 3c. Analytical data of Aspen Basin migmatite paleosome (sample 01-02P) zircon by Secondary Ion Mass Spectrometer (SIMS).

Sample ID	$^{206}Pb/^{238}U$ age	age error (1σ)	$^{207}Pb/^{235}U$ age	age error (1σ)	$^{207}Pb/^{206}Pb$ age	age error (1σ)		$^{207}Pb/^{235}U$	1σ error	$^{206}PB/^{238}U$	1σ error	rho	$^{207}Pb/^{206}Pb$	1σ error	$^{204}Pb/^{206}Pb$	1σ error	U/Th	U ppm	Th ppm
01-02Pa-01	1701	54	1665	30	1620	14	99.2	4.155	0.151	0.3021	0.0108	0.98	0.09978	0.00073	0.00043	0.00004	0.175	730	127
01-02Pa-02	2131	73	2075	36	2020	10	99.5	6.72	0.271	0.3917	0.0157	0.99	0.1244	0.0007	0.00026	0.00003	0.032	1500	48
01-02Pa-03	1671	59	1669	35	1667	22	99.5	4.177	0.177	0.296	0.0119	0.96	0.1024	0.0012	0.00029	0.00007	0.637	230	146
01-02Pa-04	1106	39	1291	30	1611	24	97.0	2.564	0.105	0.1872	0.0072	0.95	0.09932	0.00129	0.00160	0.00008	0.417	1600	667
01-02Pa-05	1516	67	1573	40	1650	19	99.0	3.706	0.183	0.265	0.0131	0.98	0.1014	0.001	0.00055	0.00007	0.638	800	510
01-02Pa-06	1548	60	1491	35	1410	37	97.9	3.341	0.152	0.2714	0.0119	0.91	0.08926	0.00174	0.00110	0.00010	0.106	630	67
01-02Pa-07	815	31	1002	27	1438	22	97.8	1.684	0.07	0.1348	0.0055	0.96	0.0906	0.00106	0.00116	0.00007	0.037	2900	107

Table 4. Chemisty of Aspen Basin migmatite (sample 01-02) zircon by Electron Probe Microanalyzer (EPMA).
L (leucosome), M (melanosome), and P (paleosome).

Sample ID	Type	Cr_2O_1	FeO	MoO_3	ZrO_2	TiO_2	CaO	Al_2O_3	HfO_2	SiO_2	Total	Th/U	U ppm	Th ppm
01-02Lb-03c	L	0	0.0031	0	65.9929	0.3593	0.0099	0.0722	1.5007	32.4164	100.3544	0.029	2300	68
01-02Lb-04c	L	0	0.0447	0	65.0415	0	0.0365	0	1.9308	32.543	99.5965	0.005	1100	6
01-02Lb-04cc	L	0	0.8194	0	64.3899	0	0.0228	0.4306	1.845	32.4408	99.9486	0.010	2900	29
01-02Lb-05c	L	0	0.7416	0	52.6853	1.2787	1.8186	1.3222	2.6512	30.6171	91.1148	0.020	9300	185
01-02Lb-05r	L	0	1.0523	0	58.2327	0.1994	1.1734	0.1159	2.4183	30.6501	93.8422	0.017	8500	143
01-02Lb-06c	L	0	0.1562	0	59.4034	1.6772	1.1989	0.3905	1.8734	30.9426	95.6423	0.025	6000	151
01-02Lb-06r	L	0	0.062	0	64.9466	0	0.2342	0.5619	1.846	33.0774	100.728	0.036	3000	108
01-02Lb-07r	L	0	0.0202	0	67.7089	1.3572	0.0446	0	1.0364	35.0725	105.2398	0.110	490	54
01-02Lb-08c	L	0	0.1316	0	58.7515	1.6762	1.3704	0.1485	2.705	31.3537	96.1369	0.046	2500	116
01-02Lb-08r	L	0	0.0563	0	62.1323	2.1118	0.541	0	3.2607	32.1116	100.2136	0.022	3500	77
01-02Mb-03c	M	0	0.0176	0	66.3611	0.1989	0.0131	0	1.3256	33.1448	101.061	0.481	550	265
01-02Mb-07c	M	0	0.0272	0	68.6725	0	0.0116	0.0454	1.4802	33.3662	103.6031	0.041	820	34
01-02Mb-12c	M	0	0.1203	0	64.0715	1.156	0.0017	0.0071	1.4152	32.8862	99.6581	0.060	1600	96
01-02Pa-2	P	0	0.1202	0	62.553	0	0.2455	0.0039	1.6775	32.025	96.6252	0.032	1500	48
01-02Pa-4	P	0	0	0	64.4261	0.1199	0.0153	0	1.1622	32.938	98.6616	0.417	1600	667
01-02Pa-5	P	0	0.0571	0	63.8879	0	0.0155	0.0805	1.098	32.0057	97.1448	0.638	800	510
01-02Pa-6	P	0	0.0616	0	66.1671	0.6926	0.0075	0.0579	1.1218	33.5534	101.6618	0.106	630	67

FIGURES

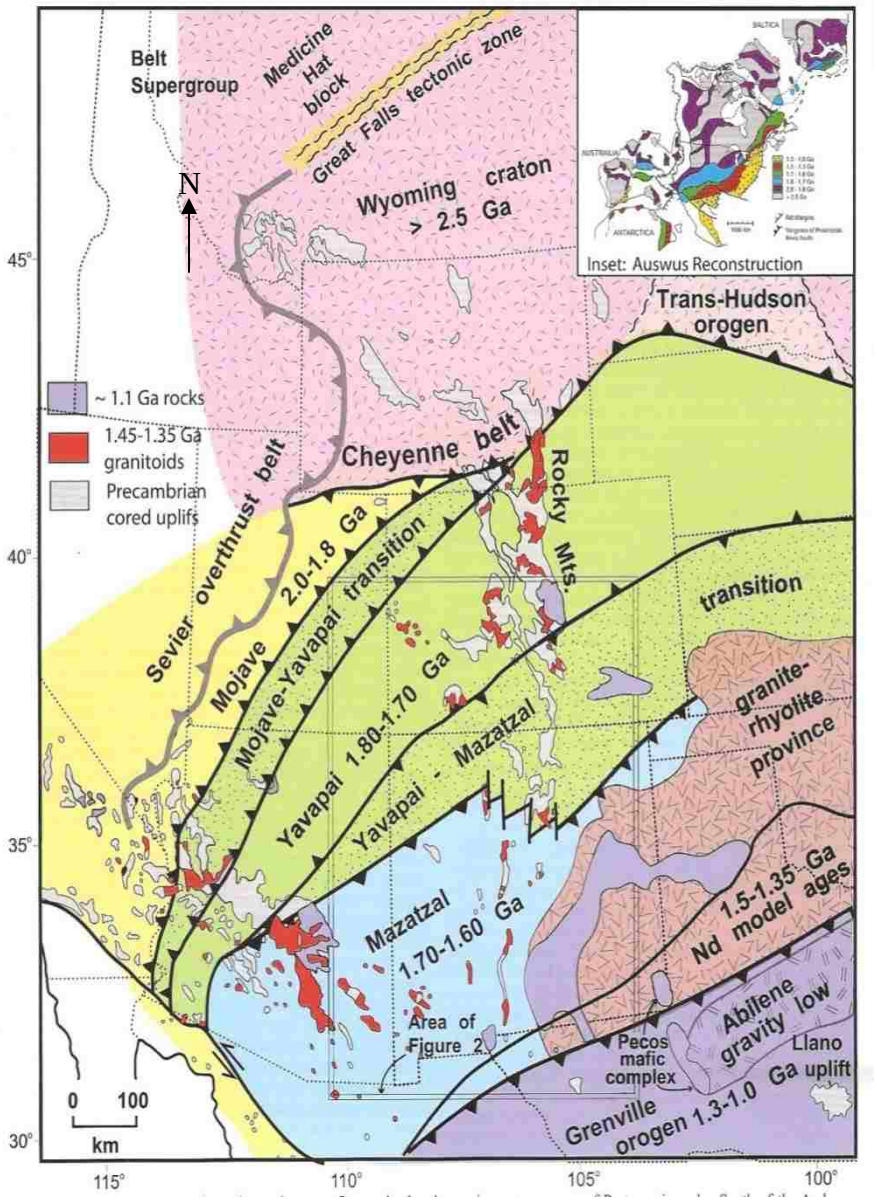

Figure 1. Proterozoic crustal provinces in southwestern Laurentia include the (1) 2.0 Ga to 1.8 Ga Mojave province of accretionary arcs on older crust; (2) 1.8 Ga to 1.7 Ga Yavapai province comprised primarily of juvenile arc crust; and (3) 1.7 Ga to 1.6 Ga Mazatzal province of juvenile crust (Karlstrom et al., 2004; Karlstrom et al., 2001).

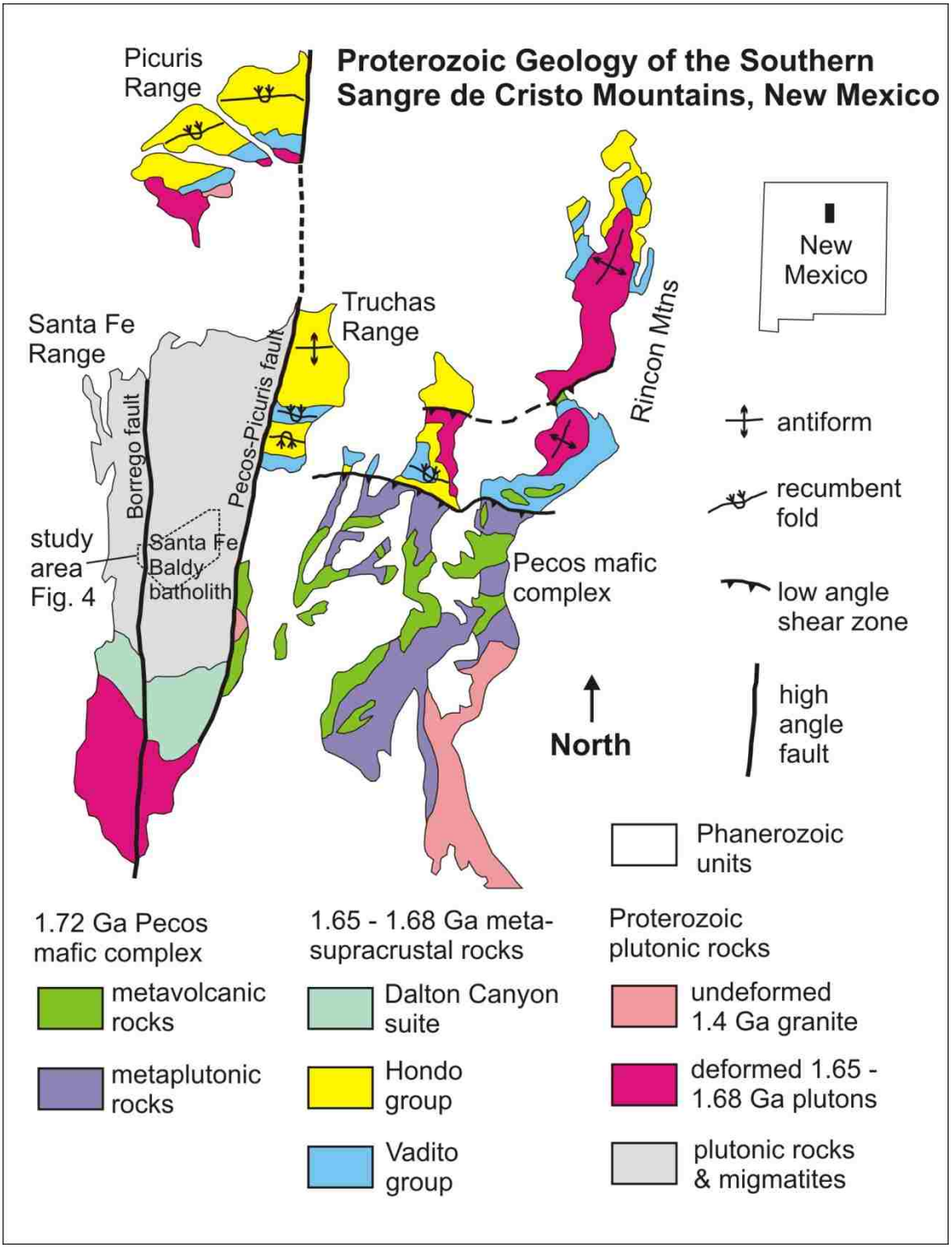

Figure 2. General map of Proterozoic geology of the Sangre de Cristo Mountains in northern New Mexico (from Karlstrom et al., 2004). (Aspen Basin study area indicated is shown in more detail in figure 4.)

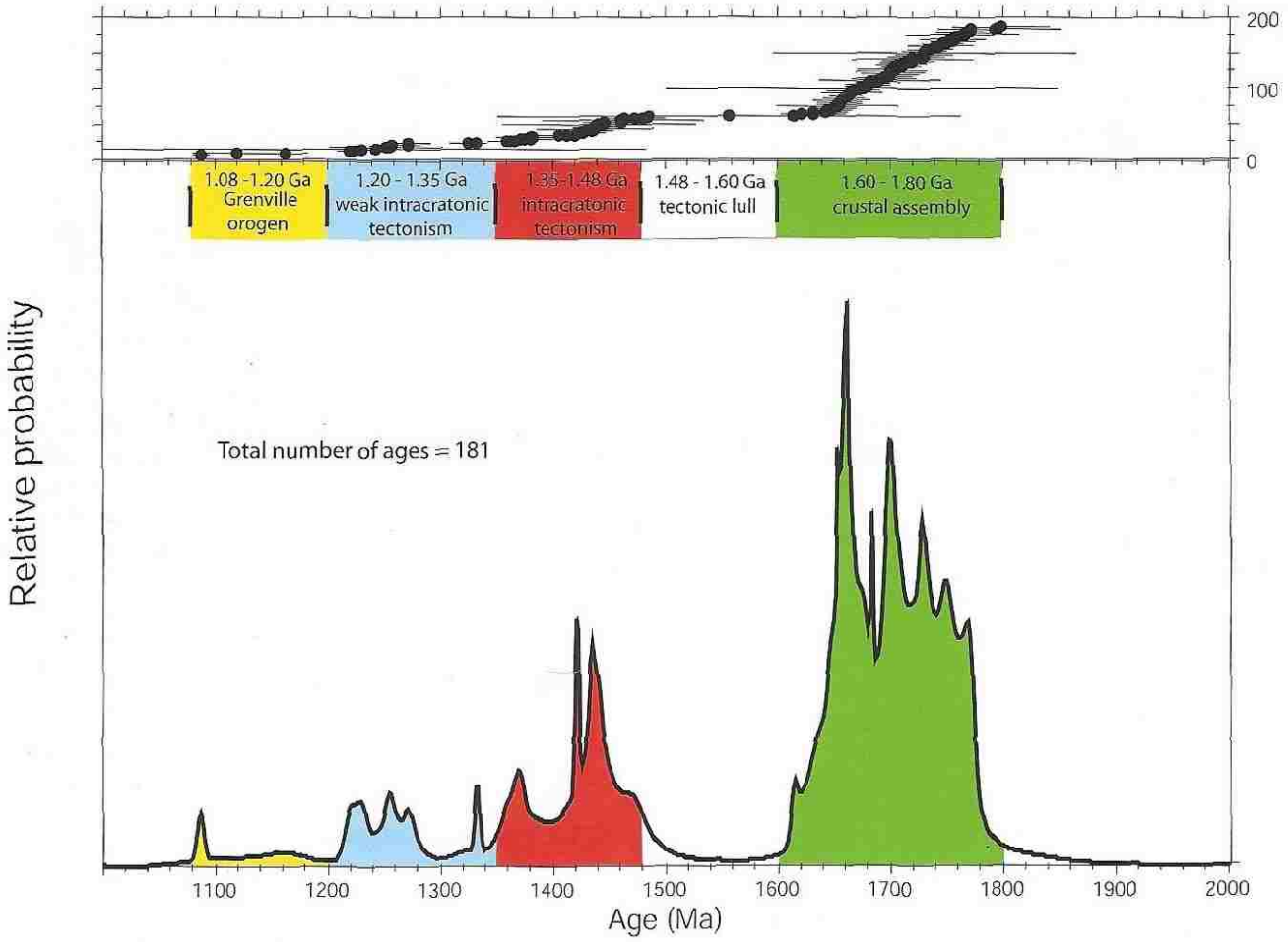

Figure 3. U-Pb probability plot of zircon ages from New Mexico (Karlstrom et al., 2004). Ages are reported at the top of the figure, shown as black data points with error bars at 2σ. The total number of zircon ages reported is 181. This plot illustrates the timing of deformational, metamorphic, and tectonic events within the New Mexico region; 1.80 – 1.60 Ga crustal assembly (green) involving the Yavapai and Mazatzal crustal provinces is separated from 1.48 – 1.35 Ga intracratonic tectonism (red) and emplacement of ~1.4 Ga anorogenic granites by a tectonic lull (white) from 1.60 – 1.48 Ga. Weak intracratonic tectonism (blue) occurs from approximately 1.35 – 1.20 Ga and the Grenville orogeny (yellow) occurs from approximately 1.20 – 1.08 Ga.

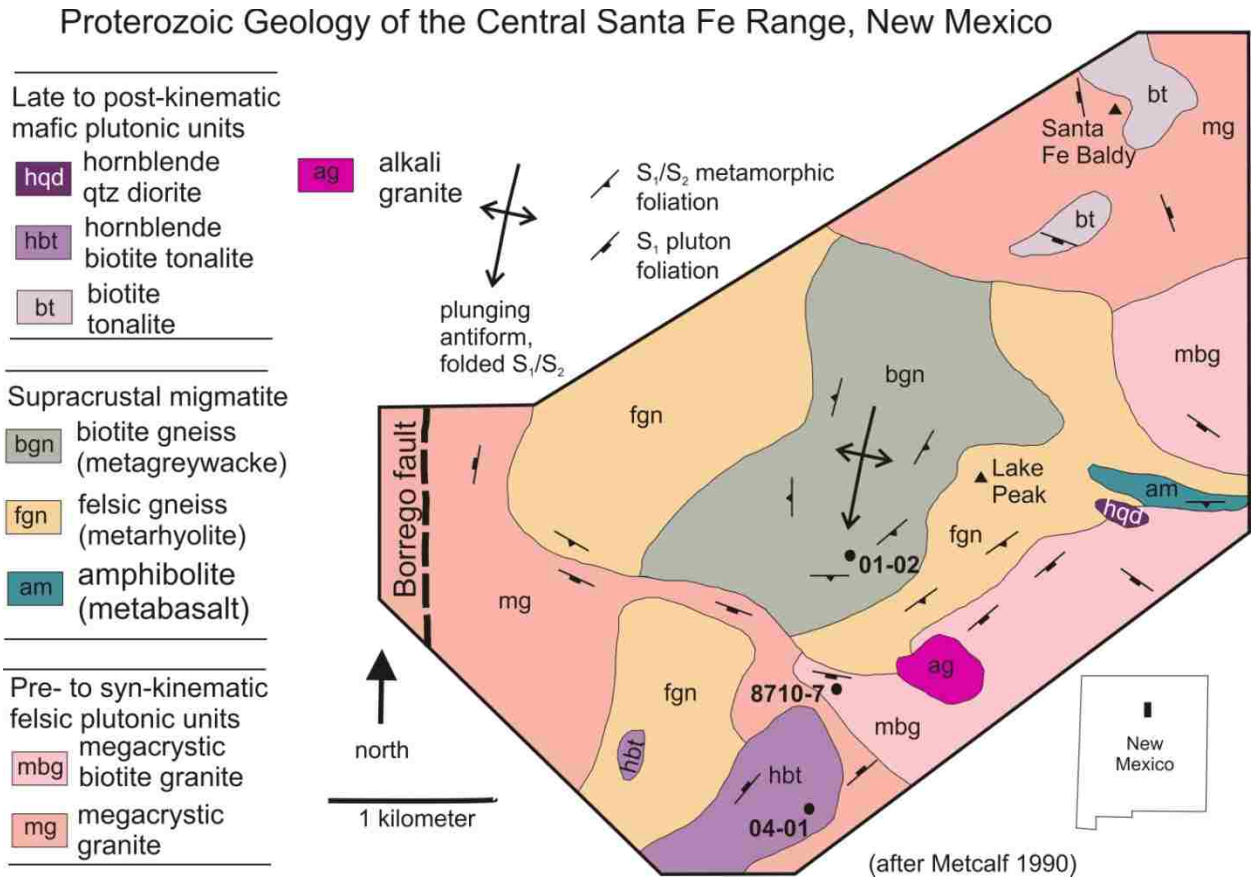

Figure 4. General map of Proterozoic geology of the Santa Fe Range, NM modified from Figure 2 (Metcalf, 1990). Lithologic units were mapped, by Metcalf (1990), into three groups; (1) pre- to syn-kinematic felsic plutonic units, (2) syn-kinematic supracrustal migmatites and (3) late to post-kinematic mafic plutonic units. Sample materials used in this study include the (1) megacrystic biotite granite (mbg), (2) biotite gneiss (bgn) and (3) hornblende biotite tonalite (hbt) units.

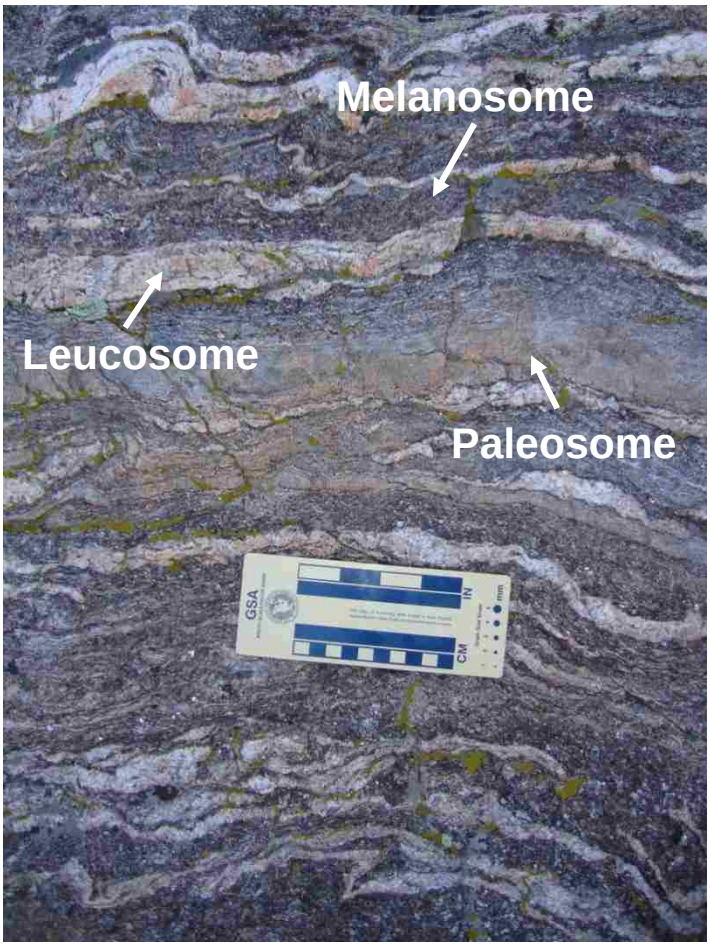

Figure 5. Image of Aspen Basin migmatite (sample 01-02), illustrating migmatite morphology that includes the paleosome (protolith), leucosome (solidified anatectic melt), and melanosome (residual solids).

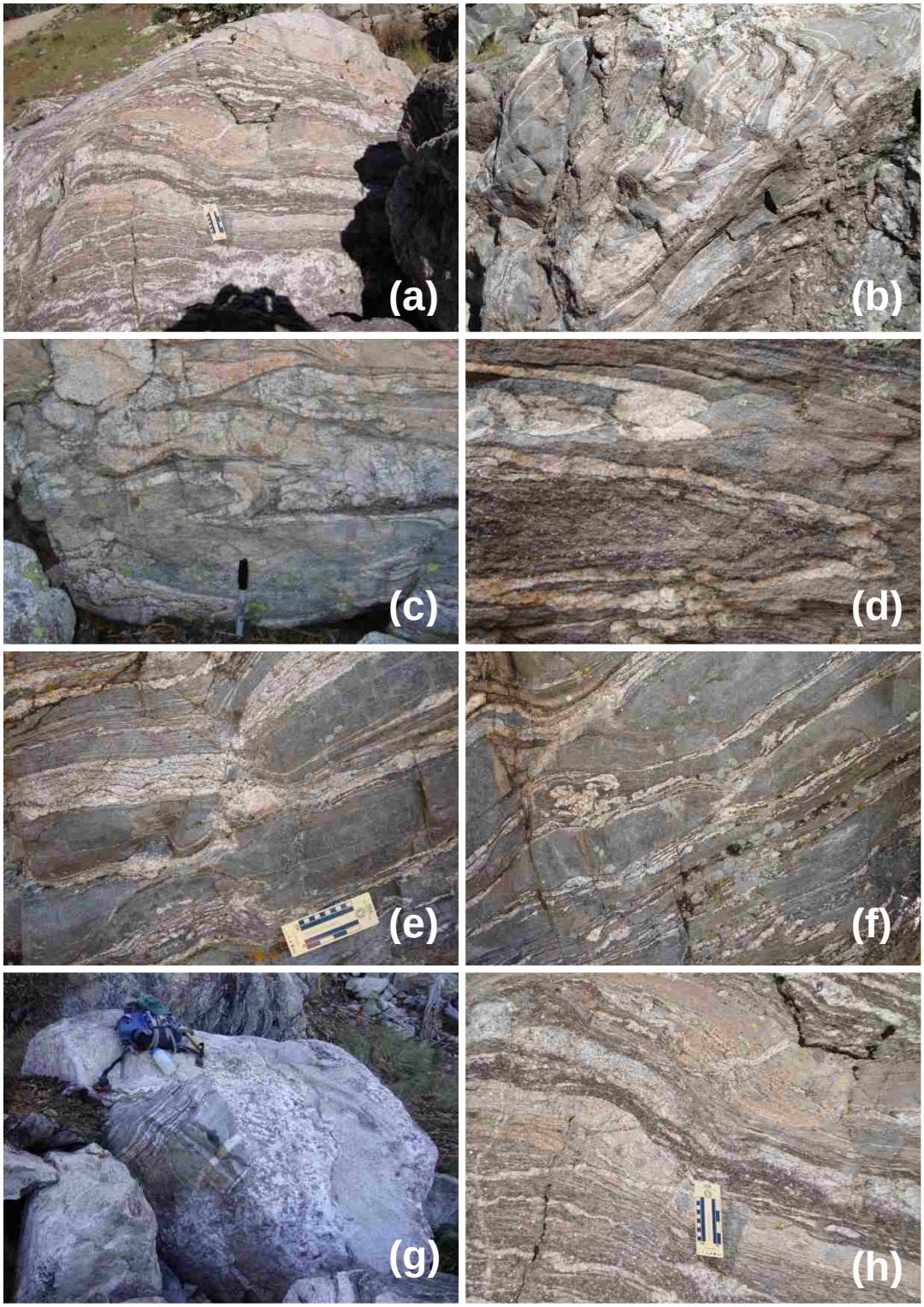

Figure 6. Syn-kinematic structures seen in the Aspen Basin migmatites include: (a) in-situ compositional layering, (b & c) tight to isoclinal, intrafolial folds and (d) parasitic folds, (e & f) boudinage features, and (g & h) leucocratic veins and dikes.

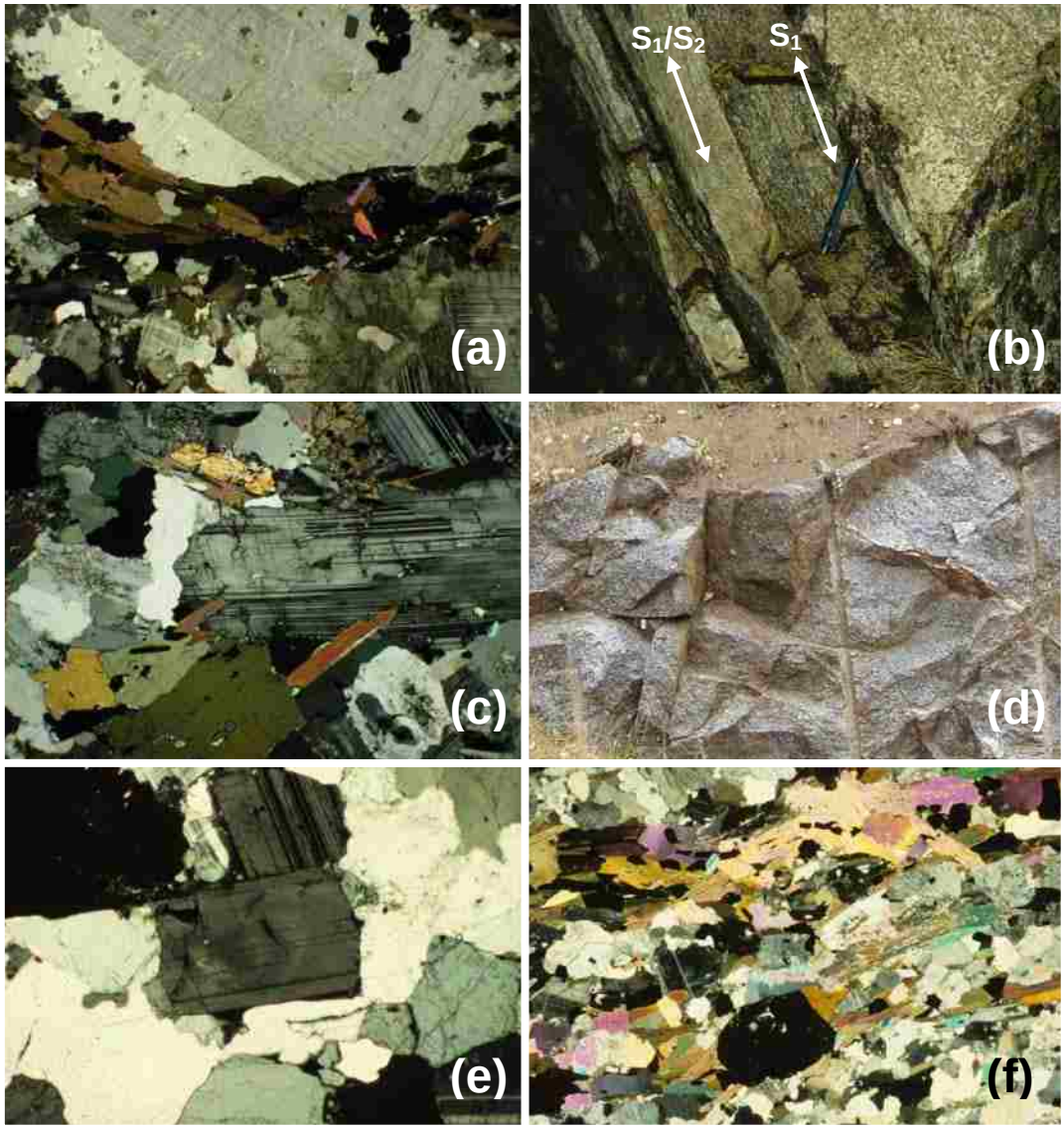

Figure 7. Thin section and field photographs of sample materials; megacrystic biotite granite (mbg; sample 8510-7) (a & b), hornblende biotite tonalite (hbt; sample 04-01)) (c & d), and Aspen Basin migmatite (bgn; sample 01-02) (e & f: thin section only, see Figures 5 & 6 for field images) from Santa Fe range, northern New Mexico; (a) oriented plagioclase and microcline megacrysts and biotite mats (S_1) in mbg; (b) S_1 fabric in mbg is parallel to composite S_1/S_2 fabric of bgn where discordant leucosomes cross-cut both S_1 and S_1/S_2 fabrics; (c) random orientation of plagioclase and biotite grains is common in hbt; (d) outcrop of hbt (crosscuts both mbg and bgn); (e) thin section image of leucosome displaying coarse texture and lack of internal foliations and (f) melanosome displaying a strong mica grainshape foliation defined by the alignment of micas.

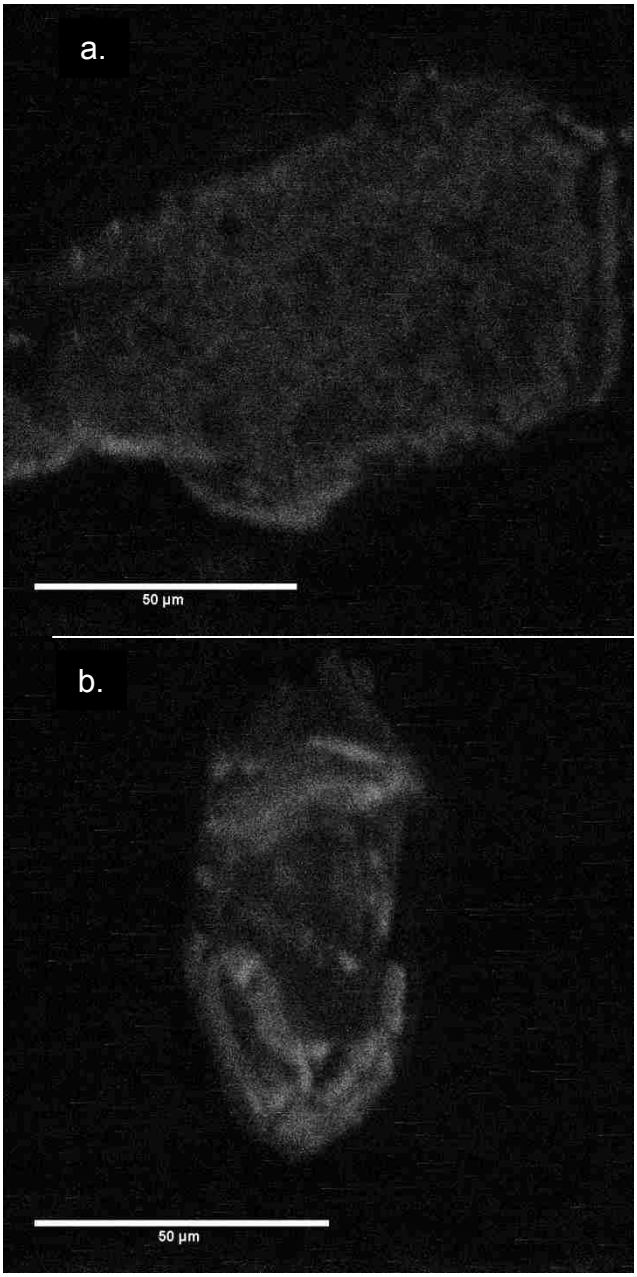

Figure 8. Cathodoluminescence (CL) imagery of migmatite zircon from sample 079-3. (a) Leucosome (079-3L) and (b) melanosome (079-3M) zircon yield poor quality images that are interpreted to be the result of high uranium contents paired with radiation damage of zircon caused by the decay of U- and Th-series elements. Dark-grey areas of low luminescence are also attributed to transgressive recrystallization fronts that formed through hydrothermal alteration of zircon by late-stage fluids and/or melts in the solid-state.

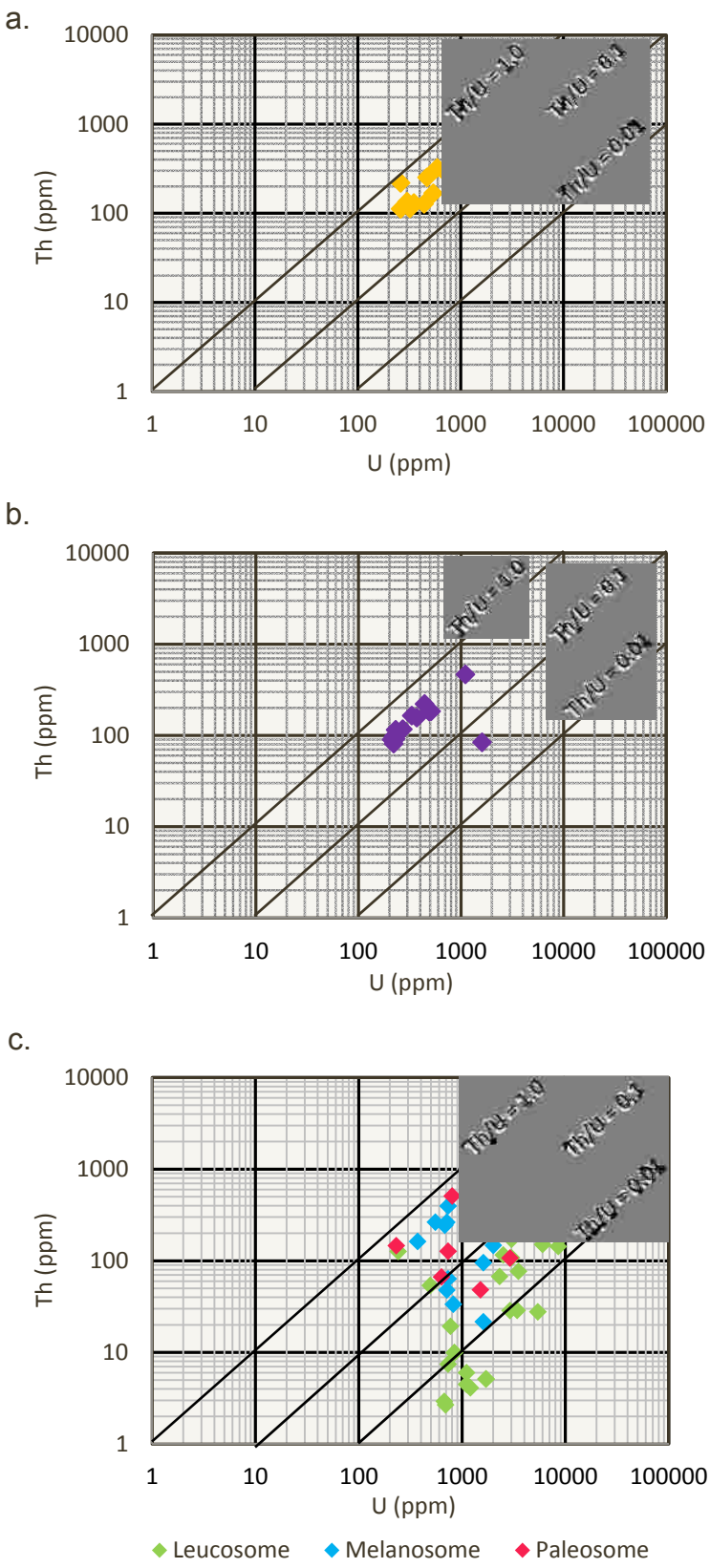

Figure 9. Th vs. U plot for (a) pre-kinematic granite, (b) post-kinematic tonalite, and (c) Aspen Basin migmatite.

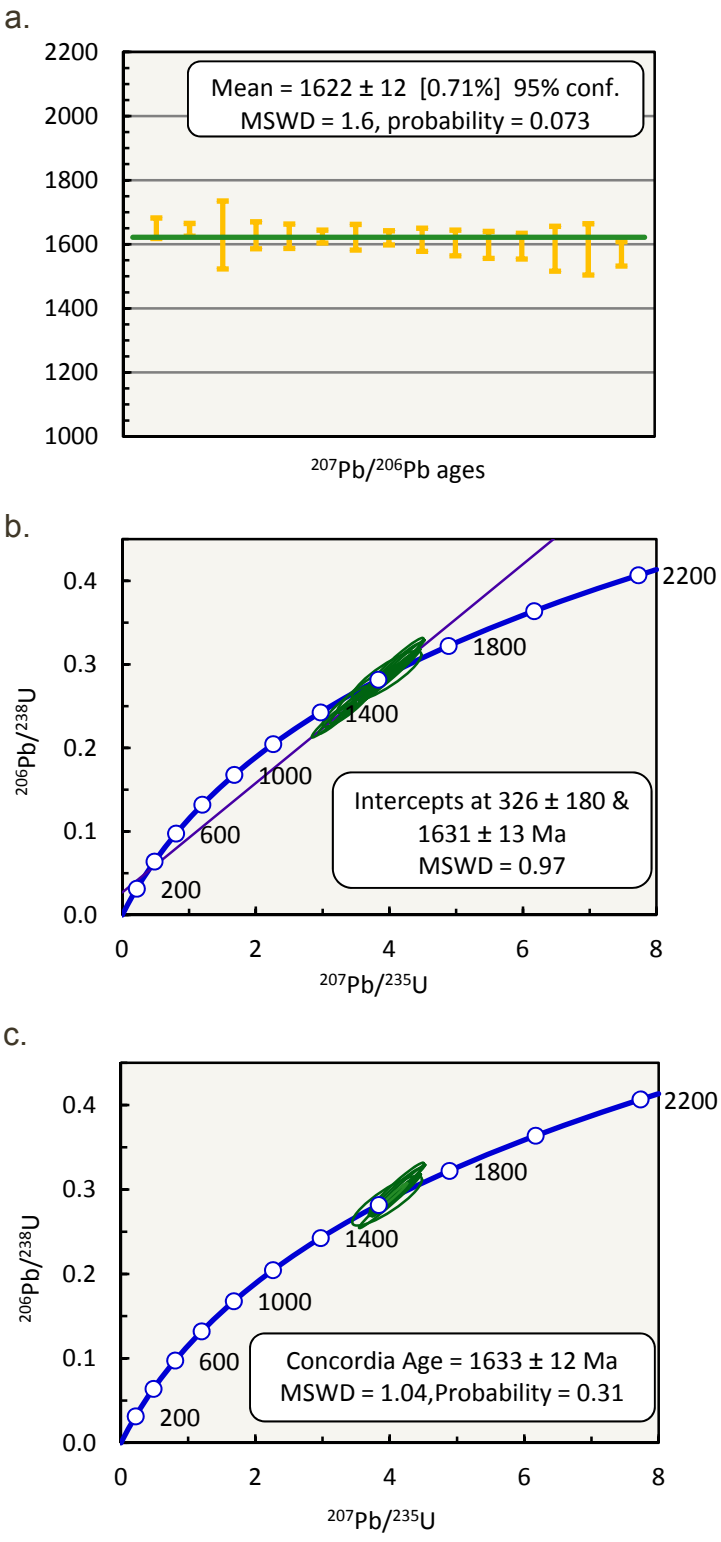

Figure 10. Weighted average (a) and concordia diagram of all zircon analyses (b) and concordia diagram of concordant zircon analyses (c) for pre-kinematic megacrystic biotite granite. All data-point error symbols and ellipses are 2-sigma.

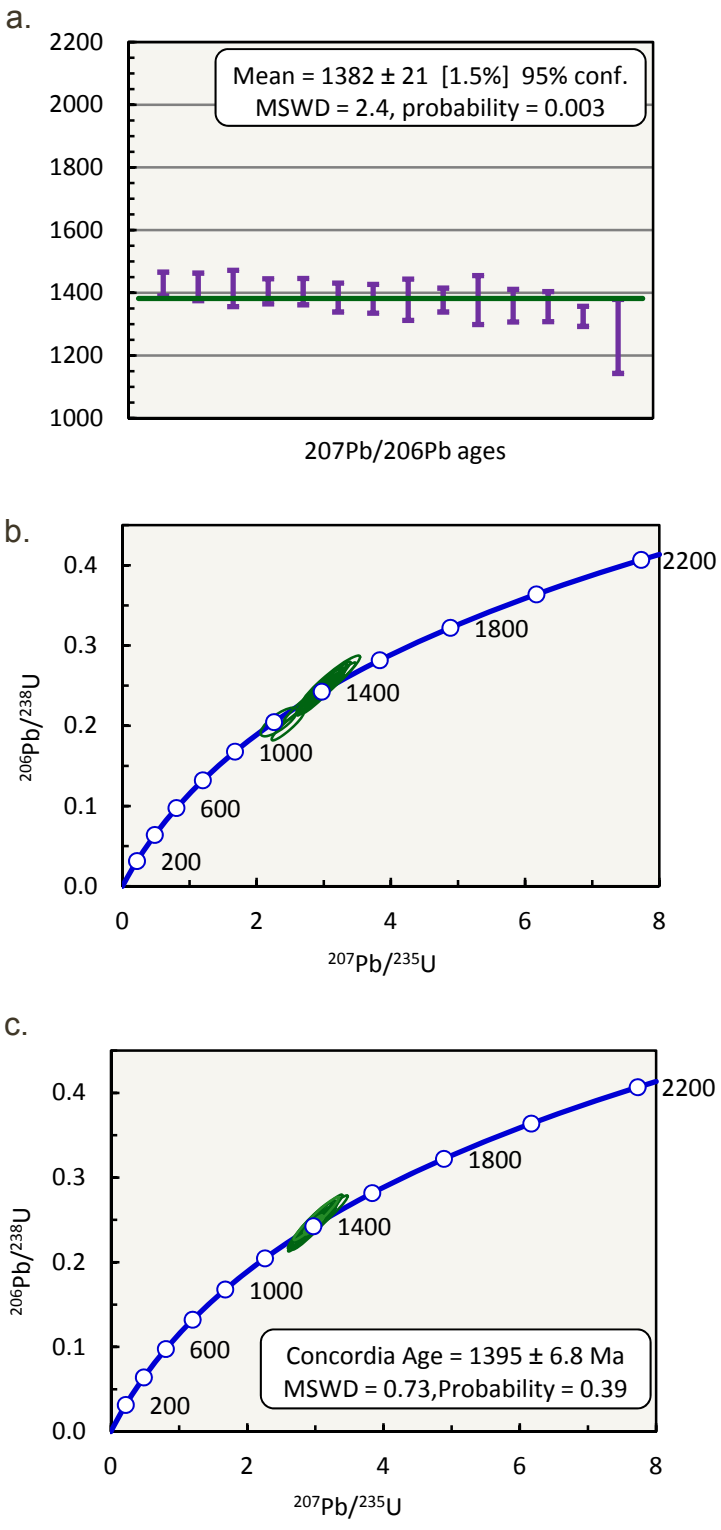

Figure 11. Weighted average (a) and concordia diagram of all zircon analyses (b) and concordia diagram of concordant zircon analyses (c) for post-kinematic hornblende biotite tonalite. All data-point error symbols and ellipses are 2-sigma.

a.

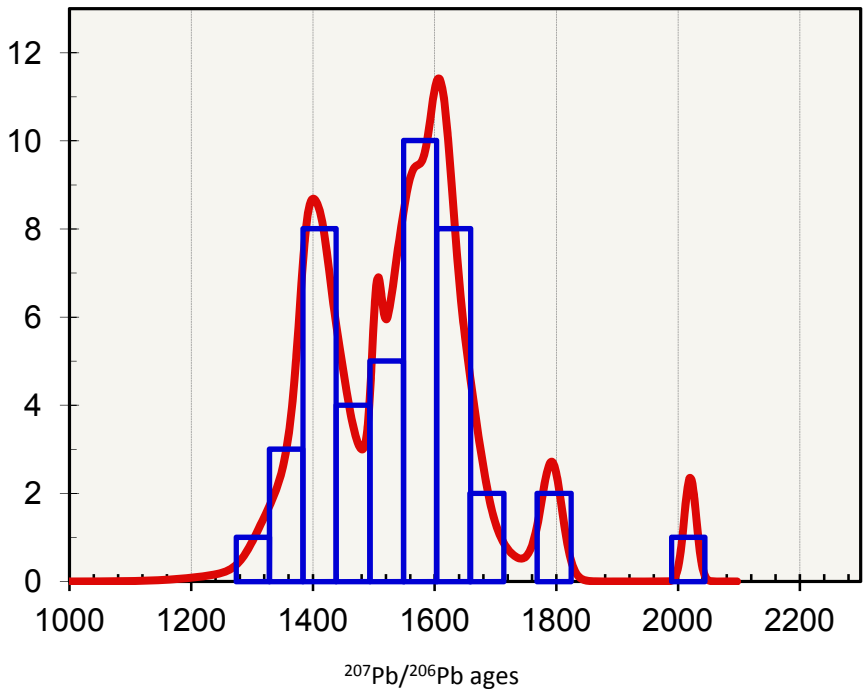

b.

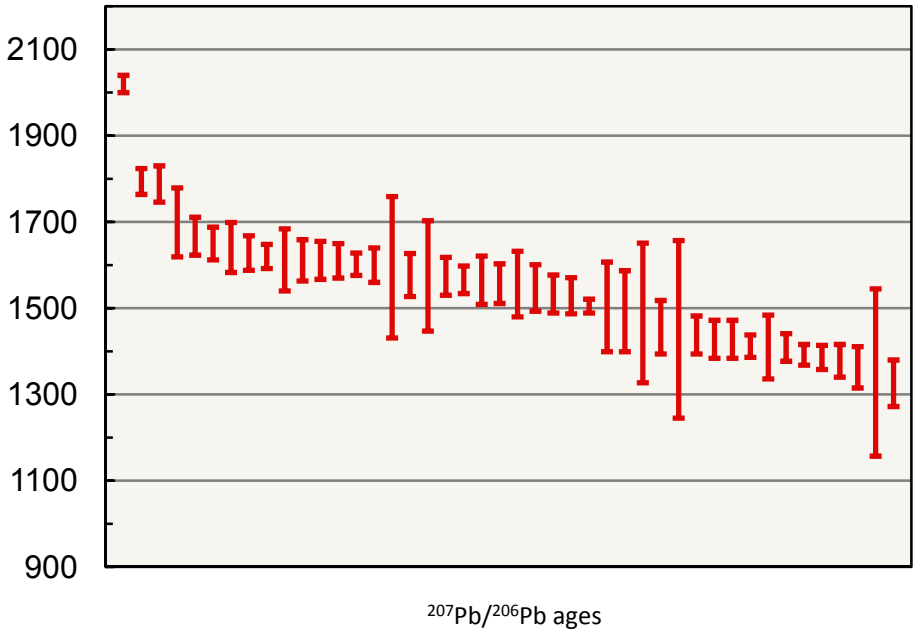

Figure 12. Relative probablility (a) and weighted average (b) age populations of all migmatite samples for Aspen Basin migmatite. Data point error symbols are 2-sigma.

a.

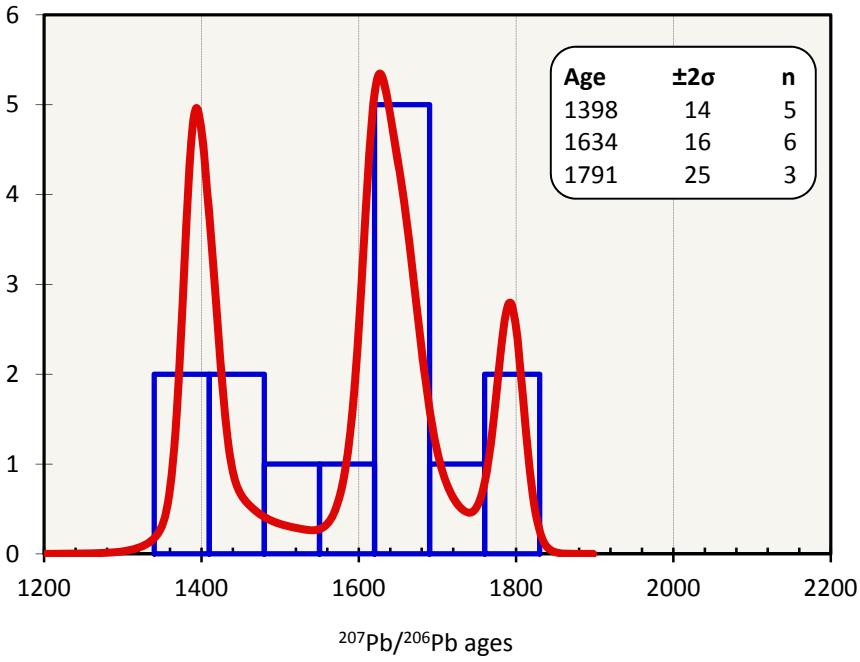

b.

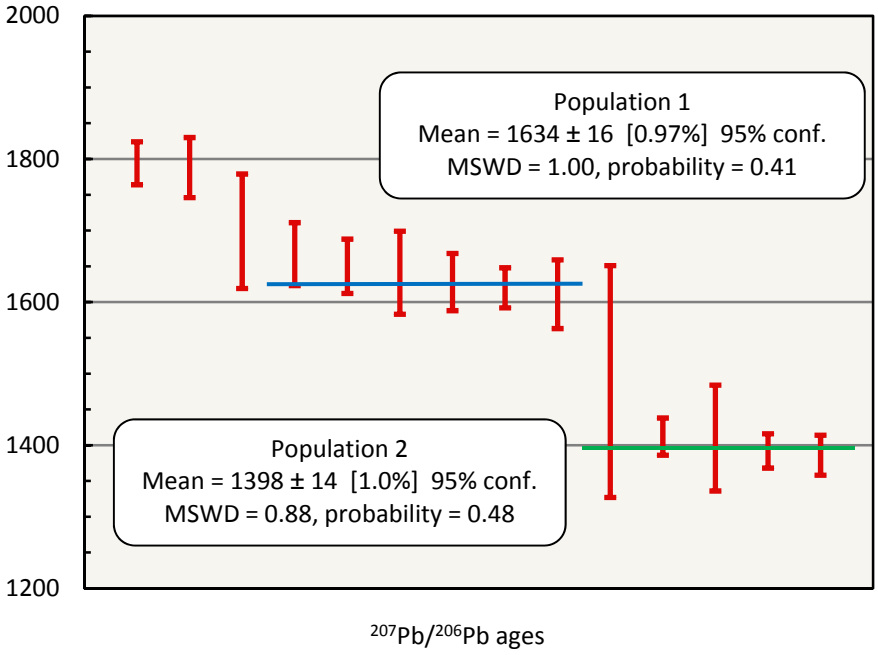

Figure 13. Relative probablility (a) and weighted average (b) age populations of Th/U ratios >0.1 for Aspen Basin migmatite zircon. Data point error symbols are 2-sigma. Population 1 represents zircon inheritance at 1634 ± 16 Ma and population 2 represents new growth zircon at 1398 ± 14 Ma. Three additional analyses yield zircon inheritance at 1791 ± 25 Ma.

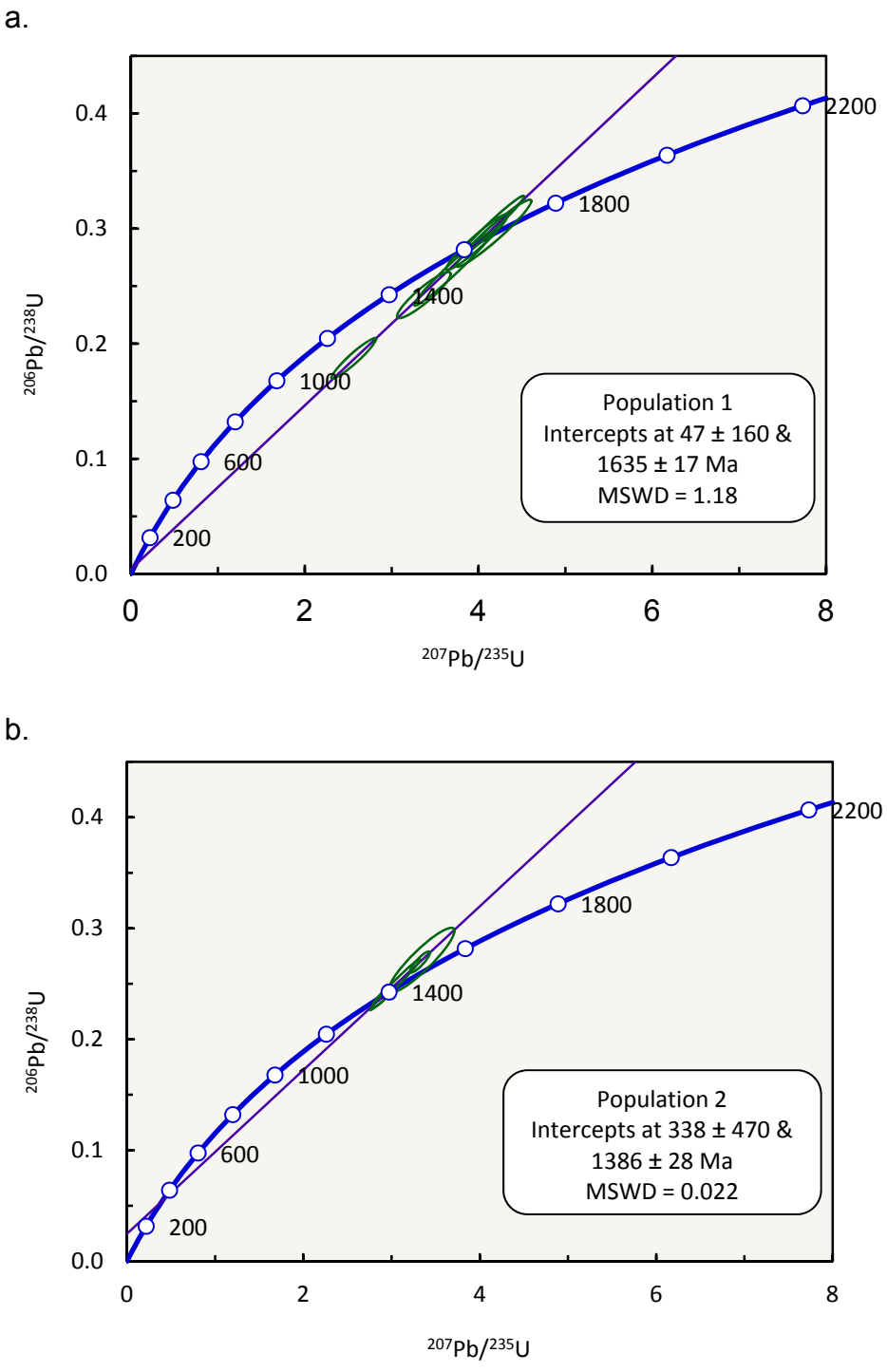

Figure 14. Concordia plots of (a) population 1 (inherited protolith zircon) and (b) population 2 (new growth zircon), with Th/U >0.1 for Aspen Basin migmatite zircon. Data point error ellipses are 2-sigma.

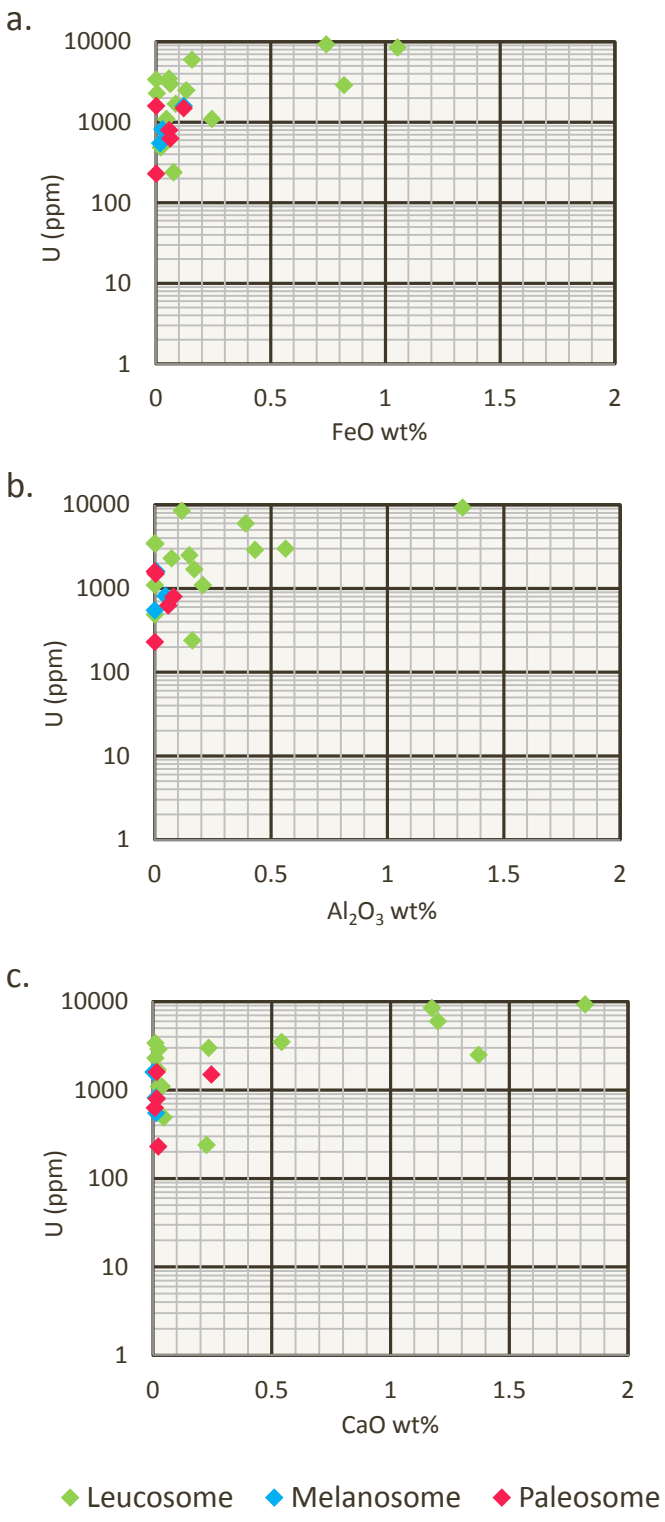

Figure 15. EPMA data plots of FeO, Al_2O_3, and CaO versus U (ppm) for leucosome (sample 01-02L), melanosome (sample 01-02M) and paleosome (sample 01-02P).

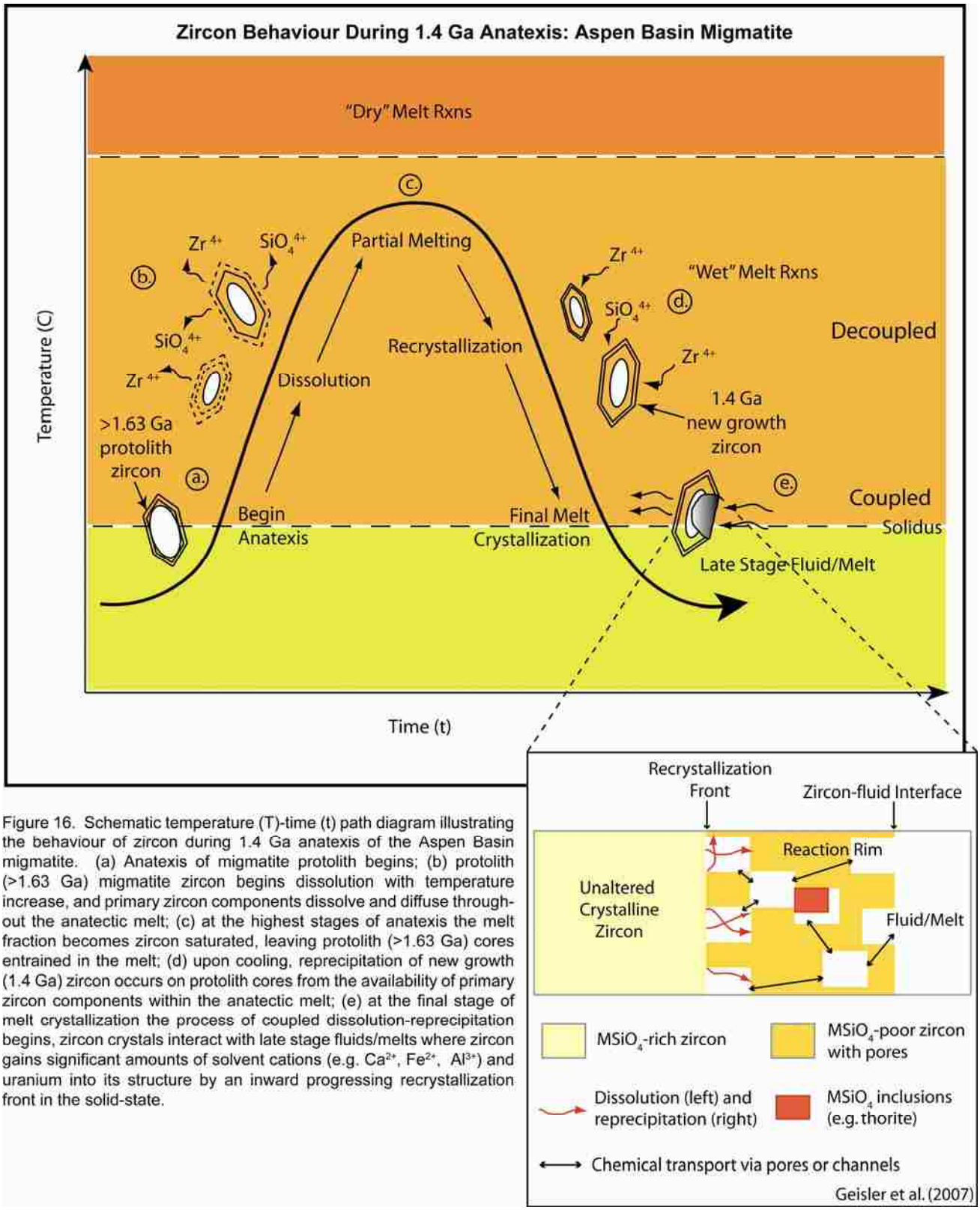

Figure 16. Schematic temperature (T)-time (t) path diagram illustrating the behaviour of zircon during 1.4 Ga anatexis of the Aspen Basin migmatite. (a) Anatexis of migmatite protolith begins; (b) protolith (>1.63 Ga) migmatite zircon begins dissolution with temperature increase, and primary zircon components dissolve and diffuse throughout the anatectic melt; (c) at the highest stages of anatexis the melt fraction becomes zircon saturated, leaving protolith (>1.63 Ga) cores entrained in the melt; (d) upon cooling, reprecipitation of new growth (1.4 Ga) zircon occurs on protolith cores from the availability of primary zircon components within the anatectic melt; (e) at the final stage of melt crystallization the process of coupled dissolution-reprecipitation begins, zircon crystals interact with late stage fluids/melts where zircon gains significant amounts of solvent cations (e.g. Ca^{2+}, Fe^{2+}, Al^{3+}) and uranium into its structure by an inward progressing recrystallization front in the solid-state.

BIBLIOGRAPHY

Anderson, J. L. and Bender, E. E. (1989) Nature and origin of Proterozoic A-type granite magmatism in the southwestern United States. Lithos, v. 23, pp. 19-52.

Anderson, J. L. (1989) Proterozoic anorogenic granites of the southwestern United States, *in* Jenny, J. P. and Reynolds, S. J., eds., Geologic evolution of Arizona. Tucson, Arizona Geological Society Digest, pp. 211-238.

Anderson, J. L. (1983) Proterozoic anorogenic granite plutonism of North America, *in* Medaris, L. G., Jr., Beyers, C. W., Mickelson, D. M., and Shanks, W. C., eds., Proterozoic geology. Selected papers from an International Proterozoic Symposium: Geological Society of America, Memoir 161, pp. 133-154.

Ashworth, J. R. (1985) Introduction: in Migmatites. Blackie and Son, Glasgow, United Kingdom (GBR), 1-35.

Bauer, P. W. and Williams, M. L. (1994) Late tectonic intrusion in the Magdalena Mountains: Evidence for Early Proterozoic deformation in central New Mexico. Precambrian Research, v. 67, pp. 349-356.

Bauer, P. W. et al. (1993) Proterozoic plutonism and regional deformation: New constraints from the southern Manzano Mountains, central New Mexico. New Mexico Geology, v. 15, pp. 49-55.

Bea, F. and Montero, P. (1999) Behavior of accessory phases and redistribution of Zr, REE, Y, Th, and U during metamorphism and partial melting of metapelites in the lower crust: An example from the Kinzigite Formation of Ivrea-Verbano, NW Italy. Geochimica et Cosmochimica Acta, v. 63, no. 718, pp. 1133-1153.

Bishop, J. L. (1997) The determination of a quantitative P-T-t-D history for Proterozoic rocks of the Cerro Colorado area, north central New Mexico (M.S. thesis). Amherst, University of Massachusetts, p. 91.

Carson, C. J. et al. (2002a) U-Pb isotopic behavior of zircon during upper-amphibolite facies fluid infiltration in the Napier Complex, east Antarctica. Earth and Planetary Science Letters, v. 199, pp. 287-310.

Daniel, C. G. et al. (1995) The reconstruction of a middle Proterozoic orogenic belt in north-central New Mexico, U.S.A. New Mexico Geological Society Guidebook, 46th Field Conference, Geology of the Santa Fe Region, pp. 193-200.

Geisler, T. et al. (2007) Re-equilibration of Zircon in Aqueous Fluids and Melts. Elements, v. 3, pp. 43-50.

Harley, S. L. et al. (2007) Zircon Behaviour and the Thermal Histories of Mountain Chains. Elements, v. 3, pp. 25-30.

Harley, S. L. et al. (2001) Zircon chemistry and the definition of events in Archaean granulite terrains. In: Cassidy, K. F., Dunphy, J. M., van Kranendonk, M. J. (eds.) Extended Abstracts of 4th International Archaean Symposium. AGSO-Geoscience Australia Record 2001/37, Canberra, pp. 511-513.

Harrison, T. M. and Watson, E. B. (1983) Kinetics of zircon dissolution and zirconium diffusion in granitic melts of variable water content. Contrib. Mineral. Petrol., v. 84, pp. 67-72.

Hoskin, P. and Black, L. (2000) Metamorphic zircon formation by solid-state recrystallization of protolith igneous zircon. J. metamorphic Geol., v. 18, pp. 423-439.

Ireland, T. R. and Williams, I. S. (2003) Considerations in zircon geochronology by SIMS. Mineral. Soc. Am. Rev. Mineral. and Geochem., v. 53, pp. 215-241.

Johannes, W. (1985) The significance of experimental studies for the formation of migmatites, *in* Ashworth, J. R., eds., Migmatites. Blackie, Glasgow, U. K., pp. 36-85.

Karlstrom, K. E. et al. (2004) Proterozoic tectonic evolution of the New Mexico region: A synthesis. The Geology of New Mexico, A Geologic History, New Mexico Geological Society, pp 1-34.

Karlstrom, K. E. et al. (2001) Geology of the Capilla Peak 7.5-minute quadrangle, Torrance and Valencia Counties, New Mexico. New Mexico Bureau of Mines and Mineral Resources, Openfile Digital Geologic Map OF-DM-27, scale 1:24,000.

Karlstrom, K. E. and Humphreys, E. D. (1998) Persistent influence of Proterozoic accretionary boundaries in the tectonic evolution of southwestern North America: Interaction of cratonic grain and mantle modification events. Rocky Mtn. Geo., v. 33, no. 2, pp. 161-179.

Karlstrom, K. E. and Bowring, S. A. (1993) Proterozoic orogenic history in Arizona, in Van Schmus, W. R. et al., Transcontinental Proterozoic provinces, in Reed, J. C., Jr., Bickford, M. E., Houston, R. S., Link, P. K., Rankin, D. W., Sims, P. K., and Van Schmus, W. R., eds., Precambrian: Conterminous U. S., Geo. Soc. of America, The Geology of North America, v. C-2, pp. 188-211.

Ludwig, K.R. (2008) Isoplot 3.6. A geochronological toolkit for Microsoft excel. Berkeley Geochronology Center Special Publication, no. 4, pp. 1-78.

Mehnert, K. R. (1968) Migmatites and the origin of granitic rocks. Elsevier, Amsterdam.

Metcalf, R. V. (1995) Proterozoic plutonic rocks of the central Santa Fe Range: Trace element evidence of subduction zone magmatism, north-central New Mexico. New Mexico Geological Society Guidebook, 46th Field Conference, Geology of the Santa Fe Region, pp. 185-191.

Metcalf, R. V. (1990a) Proterozoic geology of the central Santa Fe Range, New Mexico. New Mexico Geological Society, Guidebook 41, pp. 179-187.

Metcalf, R. V. (1990) Proterozoic geology of the central Santa Fe Range, northern New Mexico. New Mexico Geological Society Guidebook, 41st Field Conference, Southern Sangre de Cristo Mountains, New Mexico, pp. 179-187.

Nemchin, A. A. et al. (2001) Ostwald ripening as a possible mechanism for zircon overgrowth formation during anatexis; Theoretical constraints, a numerical model, and its application to politic migmatites of the Tickalara Metamorphics, northwestern Australia. Geochimica et Cosmochimica Acta, v. 65, no. 16, pp.2, 771-2,787.

Sawyer, E. W. (2008) Atlas of Migmatites. The Canadian Mineralogist, Special Publication 9, NRC Research Press, Ottawa, Ontario, Canada, pp. 371.

Schmitt, A. K. et al. (2003) The Geysers-Cobb Mountain Magma System, California (Part 1): U-Pb zircon ages of volcanic rocks, conditions of zircon crystallization and magma residence times. Geochimica et Cosmochimica Acta, vo. 67, no. 18, pp. 3423-3442.

Shaw, C. A. and Karlstrom, K. E. (1999 The Yavapai-Mazatzal crustal boundary in the southern Rocky Mountains. Rocky Mountain Geology, v. 34, no. 1, pp. 37-52.

Vavra, G. et al. (1999) Internal morphology, habit and U-Th-Pb microanalysis of amphibolites-to-granulite facies zircons: geochronology of the Ivrea Zone (Southern Alps). Contributions to Min. and Pet., v. 134, pp. 380-404.

Watson, E. B. and Harrison, T. M. (1983) Zircon saturation revisited: temperature and composition effects in a variety of crustal magma types. Earth Planetary Sci. Lett., v. 64, pp. 295-304.

Watt, G. R. et al. (1996) Chemical characteristics of migmatites: Accessory phase distribution and evidence for fast melt segregation rates. Contrib. Mineral. Petrol., v. 125, pp. 100-111.

Watt, G. R. and Harley, S. L. (1993) Accessory phase controls on the geochemistry of crustal melts and restites produced during water-undersaturated partial melting. Contrib. Mineral. Petrol., v. 114, pp. 550-556.

Whitmeyer, S. J. and Karlstrom, K. E. (2007) Tectonic model for the Proterozoic growth of North America. Geosphere, v. 3, no. 4, pp. 220-259.

Williams, M. L. et al. (1999) New Mexico middle-crustal cross sections: 1.65-Ga macroscopic geometry, 1.4-Ga thermal structure, and continued problems in understanding crustal evolution. Rocky Mountain Geology, v. 34, no. 1, pp. 53-66.

Williams, I. S. (1992) Some observations on the use of zircon U-Pb geochronology in the study of granitic rocks. Transactions of the Royal Society of Edinburgh, Earth Sciences 83, pp. 447-458.

Williams, M. L. (1990) Proterozoic geology of northern New Mexico: recent advances and ongoing questions. Bauer, P. W. et al., eds., Tectonic development of the Southern Sangre de Cristo Mountains, New Mexico: New Mexico Geological Society Guidebook, 41st Field Conferences, Southern Sangre de Cristo Mountains, pp. 151-159.

Wingsted, M. B. (1997) Microstructural history of the southern Picuris Range, north-central New Mexico: Implications for the nature and timing of tectonism in the southwestern United States (M.S. thesis). Amherst, University of Massachusetts, p. 119.

CURRICULUM VITA

Graduate College
University of Nevada, Las Vegas

Michelle Renee Stropky

Degree:
Associate of Science, 2006
Community College of Southern Nevada

Bachelor of Science, Environmental Geology, 2008
University of Nevada, Las Vegas

Special Honors and Awards:
Alumni Association grant – Fall 2010 to Spring 2011
Graduate and Professional Student Association grant – Spring 2010
Mineralogical Association of Canada grant – Spring 2010
Geological Society of America grant – Fall 2009
Geoscience Department scholarship – Spring 2009 and Fall 2009

Abstracts and Presentations:
Metcalf, R. V. and Stropky, M. R. (2011) U-PB Zircon Ages of Proterozoic Plutons and Migmatite, Santa Fe Range, New Mexico: Evidence of Mafic Magmatism and Syn-Kinematic Metamorphism at 1.4 Ga. Geological Society of America, Cordilleran Section (107th Annual) and Rocky Mountain Section (63rd Annual) Joint Meeting, Abstracts.

Saldana, S., Snelson, C., Taylor, W., Beachly, M., Cox, C., Davis, R., Stropky, M., Phillips, R., and Robins, C. (2008) Preliminary Pseudo 3-D Imagery of the State Line Fault, Stewart Valley, Nevada Using Seismic Reflection Data. Geological Society of America, Cordilleran Section (104th Annual) and Rocky Mountain Section (60th Annual) Joint Meeting, Abstracts.

Thesis Title:
The Behaviour of Zircon During Partial Melting in Anatectic Migmatites: Insights to Metamorphism, Deformation and Tectonism in the Central Santa Fe Range, Northern New Mexico

Thesis Examination Committee:
Chairperson, Rodney Metcalf, Ph. D.
Committee Member, Eugene Smith, Ph. D.
Committee Member, Terry Spell, Ph. D.
Graduate Faculty Representative, Vernon Hodge, Ph. D.

Organizations:
Geological Society of America (GSA)
Mineralogical Society of America (MAC)